International Journal of Heat and Mass Transfer 127 (2018) 1170–1187

Contents lists available at ScienceDirect

International Journal of Heat and Mass Transfer

journal homepage: www.elsevier.com/locate/ijhmt

Dropwise condensation on superhydrophobic nanostructure surface, part II: Mathematical model

Jian Xie [a], Jinliang Xu [a,*], Wei Shang [a], Kai Zhang [b]

[a] Beijing Key Laboratory of Multiphase Flow and Heat Transfer for Low Grade Energy Utilization, North China Electric Power University, Beijing 102206, China
[b] Beijing Key Laboratory of Emission Surveillance and Control for Thermal Power Generation, North China Electric Power University, Beijing 102206, China

ARTICLE INFO

Article history:
Received 17 April 2018
Received in revised form 19 June 2018
Accepted 2 July 2018

Keywords:
Dropwise condensation
Nanostructure
Droplet jumping
Surface wettability
Thermal resistance

ABSTRACT

Inspired by our finding that nano-grass-surface (NGS) with smaller droplets has poorer condensation heat transfer performance than smooth-single-molecule-layer surface (SSML) and the long-term operation of NGS deteriorates heat transfer to approach limit values, the secrets of droplets interacting with nano-pillars structure are explored. A comprehensive dropwise condensation model is developed. The contact angles are treated to show correct trend with respect to Cassie, partial Wenzel and Wenzel morphologies. A mixed droplet detachment model is developed to consider the coalescence-induced-jumping, rolling and sliding modes simultaneously. The maximum drop radius is $r_{max} = \min(r_{max,jump}, r_{max,roll}, r_{max,slide})$, where $r_{max,jump}$, $r_{max,roll}$ and $r_{max,slide}$ are maximum drop radii in jumping, rolling and sliding modes, respectively. The number of drop nucleation sites on NGS is f times of that on SSML, where f is the surface roughness. Our model predictions match the measured heat transfer data well. It is concluded that the dropwise condensation is the outcome of a series of positive and negative effects by introducing the nanostructure. The increased droplet population density and number of drop nucleation sites are the positive contributions, while the decreased single drop heat transfer rate and additional nanoporous thermal resistance are the negative contributions. The densely populated nano-pillars structure has the largest capability to enhance heat transfer. The Heterogeneous hydrophilicity/hydrophobicity surface limits droplet sweeping distance within neighboring hydrophilic dots, to avoid that *stone rolls on the lawn to spoil the grasses*, the heterogeneous surface is recommended to resist nanostructure failure for long-term operation.

1. Introduction

Key experimental findings in part I of this paper are summarized as: (1) Our fresh superhydrophobic nanograsses surface (NGS) keeps smaller droplets due to jumping or rolling, but still has lower heat transfer coefficients than smooth single-molecule-layer of polymer surface (SSML); (2) The long-term operation of NGS switches jumping or rolling mode to sliding mode, and heat transfer coefficients are decayed to approach limit values. Other studies also show that nanostructure surface does not always enhance condensation heat transfer [1–3]. Inspired by these findings, the objective of this paper is to explain the observed phenomena, and provide novel concept to design efficient and robust nanostructure surface for condensation. In order to do so, a comprehensive condensation heat transfer model on hydrophobic nanostructure surface should be developed. We note that the framework of dropwise condensation heat transfer model on smooth hydrophobicity surface has been established [4,5].

Condensation on hydrophobic nanostructure surface presents challenges on theoretical modeling. First, nanostructure surface may generate Cassie, partial Wenzel and Wenzel drop morphologies [6]. Because these morphologies are related to the dynamic motion of vapor-liquid interface in nano-pillars gap, and the three-phase (solid-liquid-vapor) contact point is not known in nanoscale, it is difficult to determine the morphology, which is a key factor to influence droplet growth and departure. However, depending on surface wettability, a droplet on a smooth surface behaves either Cassie or Wenzel state, which is easier to be treated. Second, nanostructure surface yields fruitful droplet detachment modes such as coalescence-induced-jumping, rolling and sliding. Even though many authors highlight the importance of jumping to condensation [7,8], no one knows the jumping contribution relative to other detachment modes. Usually, droplets detach from surface with mixed modes of jumping, rolling and sliding. Available dropwise condensation heat transfer models use the maximum drop radius based on sliding mode [9,10]. Third,

* Corresponding author.
E-mail address: xjl@ncepu.edu.cn (J. Xu).

https://doi.org/10.1016/j.ijheatmasstransfer.2018.07.008
0017-9310/

nanostructure surface introduces an additional thermal resistance of nano-porous. It is a challenge to treat this thermal resistance, especially at partial Wenzel state, because the vapor-liquid interface penetration depth in nano-porous is not known.

Kim and Kim [11] considered the increased contact angle of hydrophobic nano-structured surface on the basis of smooth hydrophobicity surface. Sikarwar et al. [10] treated the number of drop nucleation sites N_c on roughed surfaces as f times of that on smooth surface. Other studies used identical N_c on roughed surface and smooth surface [12–16]. Lee et al. [12], Kim and Nam [13] and Enright et al. [14] introduced an additional thermal resistance of the nano-structured porous layer beneath droplets. Miljkovic et al. [15] deduced the relationship between contact angle and wetting morphology of droplets and simulated the coalescence-induced-jumping of droplets on nano-structured surface. Bahrami and Saffari [16] modified the dropwise condensation model for plate surface to simulate the condensation in tubes having micro/nano structured surface on curved surface. The above investigations contribute better understanding of dropwise condensation on nano-structured surface.

In this paper, we develop a comprehensive model suitable for both flat surface without nano-structure and nano-structured surface. Our new contribution is to develop a mixed droplet detachment model linking our heat transfer model. Three maximum droplet radii are determined based on jumping, rolling and sliding independently. The mode selection criterion is written as the minimum of the three droplet sizes. We thoroughly analyze the transition and contribution of the three drop removal modes. Besides, the relationship between contact angles and droplet wetting morphologies is properly treated to show correct trend, and effect of the increased number of drop nucleation sites is also considered.

We conclude the overall heat transfer comes from a set of positive and negative contributions by using nanostructure surface instead of plain surface. The key point is to keep jumping mode for significant heat transfer enhancement. The increased number of drop nucleation sites is a positive contribution to heat transfer. The increase of contact angle maintains smaller droplets on the surface, which is beneficial to heat transfer. However, the contact angle rise worsens single drop heat transfer rate, being a negative contribution. Nano-pillars spacing is an important parameter to affect heat transfer. Heat transfer deterioration after nanostructure failure is due to the enlarged spacing size, while a densely populated nanograsses further promote condensation heat transfer.

2. Mathematical model

2.1. Framework of dropwise condensation heat transfer model

Dropwise condensation involves multi time and length scales of droplet growth, population and interactions between drop and surface structures. Condensation heat flux q is computed as

$$q = \int_{r_{min}}^{r_c} Q(r)n(r)dr + \int_{r_c}^{r_{max}} Q(r)N(r)dr \tag{1}$$

where r_{min} is the minimum drop nucleation radius, r_c is the mean average spacing between nucleation sites, r_{max} is the maximum drop radius that can stay on the surface, beyond which the drop departs. All droplets are divided into two groups: the first group with $r_{min} < r < r_c$, and the second group with $r_c < r < r_{max}$. Correspondingly, $n(r)$ is the population density of small drops having the size range of $r_{min} < r < r_c$, and $N(r)$ is the population density of large drops having the size range of $r_c < r < r_{max}$. $Q(r)$ is the heat transfer rate of a single drop having the size of r. Condensation heat transfer coefficient is written as $h = q/\Delta T$, where $\Delta T = T_s - T_w$ is the wall subcooling.

Using minimization principle of Gibbs free energy, Graham and Griffith [17] gave r_{min} as

$$r_{min} = \frac{2T_s\sigma}{\rho_l h_{lv}\Delta T} \tag{2}$$

where σ is the surface tension between vapor and liquid, T_s is the vapor saturation temperature, ρ_l is the liquid density, h_{lv} is the latent heat of evaporation. Eq. (2) gives r_{min} in nano-meter scale.

On the other hand, r_c is related to droplet nucleation site density N_c as

$$r_c = \sqrt{\frac{1}{4N_c}} \tag{3}$$

Rose [18] gave $N_c = 0.037/r_{min}^2$, but this equation is not used because N_c is overestimated [19]. Ref. [20] suggested N_c in the range of 10^9–10^{15} m^{-2}. Effect of N_c on heat transfer will be discussed later. The computation of q turns to determine heat transfer rate of a single drop $Q(r)$, droplet population densities $n(r)$ and $N(r)$ and maximum droplet radius r_{max}. We deal with flat polymer surface first, then we give a comprehensive model for nano-structure surface.

2.2. Dropwise condensation on SSML

2.2.1. Maximum droplet detachment radius r_{max}

There are several droplet removal modes on hydrophobic surface: sliding, rolling or jumping. Onset of droplet sliding and rolling is determined, followed by the determination of a mode selection criterion by coupling the criterion equations of sliding and rolling [21]. The mode selection equation tells us specific mode (sliding or rolling) once a droplet can move. Our theoretical work concludes that onset of sliding or rolling is dependent on equilibrium contact angle θ_e and contact angle hysteresis Ω, but the mode selection equation is only relied on θ_e. Three regimes are clarified: (1) $\theta_e > 147.0°$ for rolling; (2) $\theta_e < 126.3°$ for sliding; and (3) $126.3° < \theta_e < 147.0°$ for pending mode depending on Bond number.

Specifically, our condensation experiment on smooth polymer surface without nanostructure holds an equilibrium contact angle of 110°, our theoretical work concludes the sliding mode, which is consistent with our present observation. For vertical surface and neglecting shear force in low vapor velocity environment, the particular solution for onset of sliding equation yields r_{max} as

$$r_{max,slide} = \sqrt{\frac{12}{\pi^2} \times \frac{\sin\theta_e(\cos\theta_r - \cos\theta_a)}{(2 - 3\cos\theta_e + \cos^3\theta_e)} \times \frac{\sigma}{(\rho_l - \rho_v)g}} \tag{4}$$

where θ_r and θ_a are receding and advancing contact angles respectively, $\Omega = \cos\theta_r - \cos\theta_a$ represents contact angle hysteresis, ρ_v is vapor density, g is gravitational acceleration. Eq. (4) almost matches the deduction by Sikarwar et al. [10].

2.2.2. Single drop heat transfer model [19]

There are four thermal resistances for a single drop growing on SSML: interface curvature thermal resistance R_c, vapor-liquid interface thermal resistance R_i, drop thermal conduction resistance R_d, and coating layer thermal conduction resistance R_m (see Fig. 1a and b), which are:

$$R_c = \frac{2\sigma T_s}{Qr\rho_l h_{lv}} \tag{5}$$

where Q is the heat transfer rate and r is the drop radius. R_i is

$$R_i = \frac{1}{2\pi r^2 h_i(1 - \cos\theta_e)} \tag{6}$$

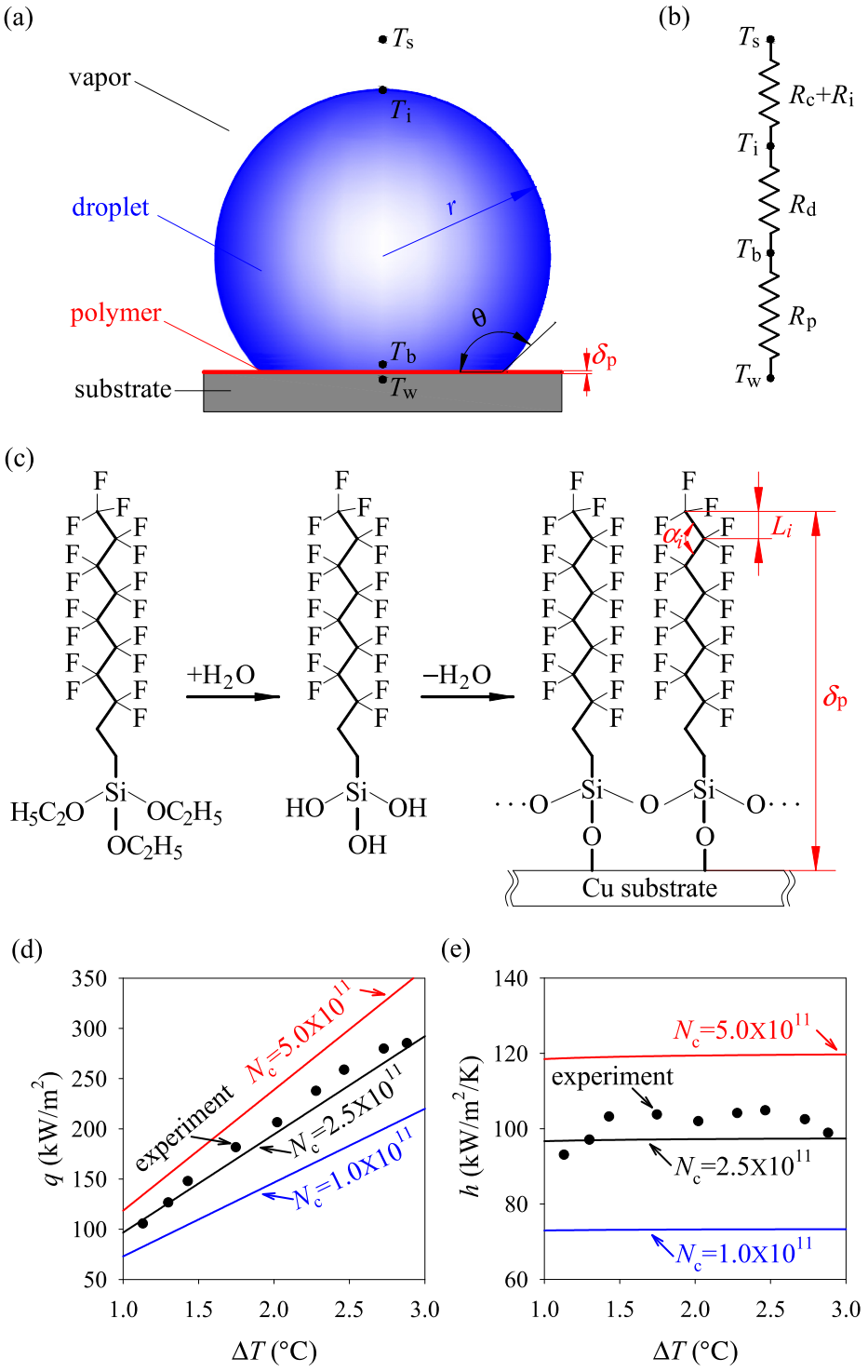

Fig. 1. Calculations of h on SSML (a and b: thermal resistance network of a single droplet; c: calculation of single-molecule-layer thickness; d: comparison of q; e: comparison of h).

where h_i is the heat transfer coefficient at vapor-liquid interface:

$$h_i = \frac{2\sigma_c}{2-\sigma_c}\sqrt{\frac{M}{2\pi RT_s}}\frac{\rho_v h_{lv}^2}{T_s} \tag{7}$$

where σ_c is the condensation coefficient, which is 1 for pure vapor condensation. R is the gas constant and M is the molecular weight. Drop conduction resistance is

$$R_d = \frac{\theta_e}{4\pi r\lambda_l \sin\theta_e} \tag{8}$$

where λ_l is the thermal conductivity of liquid. The additional coating layer resistance is

$$R_m = R_p = \frac{\delta_p}{\pi r^2 \sin^2\theta_e \lambda_p} \tag{9}$$

where λ_p is the thermal conductivity of polymer, δ_p is the polymer layer thickness. Here, the polymer layer growing on a copper substrate is described, involving two steps. The first step is the hydration of $C_{16}H_{19}F_{17}O_3Si$ polymer to expose —OH bond (see $+H_2O$ procedure in Fig. 1c). The second step is the dehydration synthesis to combine neighboring polymer chains and grow these polymer chains on the copper substrate ($—H_2O$ procedure in Fig. 1c). The growing process takes place in chain height direction. At the top of the first polymer layer, there are no extra bonds to attract second-molecule-layer of polymer, ensuring single-molecule-layer of polymer. The direct measurement of the single-molecule-layer thickness is difficult, but it can be calculated as [22]

$$\delta_p = \sum_{i=1}^{i=K} L_i \sin\left(\frac{\alpha_i}{2}\right) \tag{10}$$

where K is the number of molecular bonds, L_i is the ith molecular bond length, α_i is the molecular bond angle. Ref. [23] used Eq. (10) for the thickness calculation and found that it is sufficiently accurate compared with measurement. For this calculation, δ_p is 1 nm, which is also used by Miljkovic et al. [15] for condensation heat transfer study.

The four thermal resistances are items in a series, yielding

$$Q = \frac{T_s - T_w}{R_c + R_i + R_d + R_p} \tag{11}$$

Substituting Eqs. (5), (6), (8) and (9) into Eq. (11) gets

$$Q(r) = \frac{\pi r^2 (T_s - T_w)(1 - \frac{r_{min}}{r})}{\frac{1}{2h_i(1-\cos\theta_e)} + \frac{r\theta_e}{4\lambda_l \sin\theta_e} + \frac{\delta_p}{\pi\lambda_p \sin^2\theta_e}} \tag{12}$$

On the other hand, based on energy conservation, droplet heat transfer rate is

$$Q(r) = \frac{\pi\rho_l h_{lv}}{3}\frac{d}{dt}\left[(2+\cos\theta_e)(1-\cos\theta_e)^2 r^3\right] \tag{13}$$

Assuming droplet growing at constant contact angle, droplet growth rate G is

$$G = \frac{dr}{dt} = \frac{\left[\rho_l h_{lv}(2+\cos\theta_e)(1-\cos\theta_e)^2\right]^{-1}(T_s - T_w)\left(1 - \frac{r_{min}}{r}\right)}{\frac{1}{2h_i(1-\cos\theta_e)} + \frac{r\theta_e}{4\lambda_l \sin\theta_e} + \frac{\delta_p}{\pi\lambda_p \sin^2\theta_e}} \tag{14}$$

Defining

$$A_1 = \frac{T_s - T_w}{\rho_l h_{lv}(2+\cos\theta_e)(1-\cos\theta_e)^2} \tag{15}$$

$$A_2 = \frac{\theta_e}{4\lambda_l \sin\theta_e} \tag{16}$$

$$A_3 = \frac{1}{2h_i(1-\cos\theta_e)} + \frac{\delta_p}{\pi\lambda_p \sin^2\theta_e} \tag{17}$$

Then, Eq. (14) is simplified as

$$G = \frac{A_1}{A_2 r + A_3}\left(1 - \frac{r_{min}}{r}\right) \tag{18}$$

2.2.3. Droplet size distribution model [4,9]

In the numerical simulation, dropwise condensation droplets are divided into two groups: small droplets with $r_{min} < r < r_c$, and large droplets with $r_c < r < r_{max}$. The population balance concept was used to develop the droplet size distribution. Le Fevre and Rose [24] gave $N(r)$ formula for large drop group as

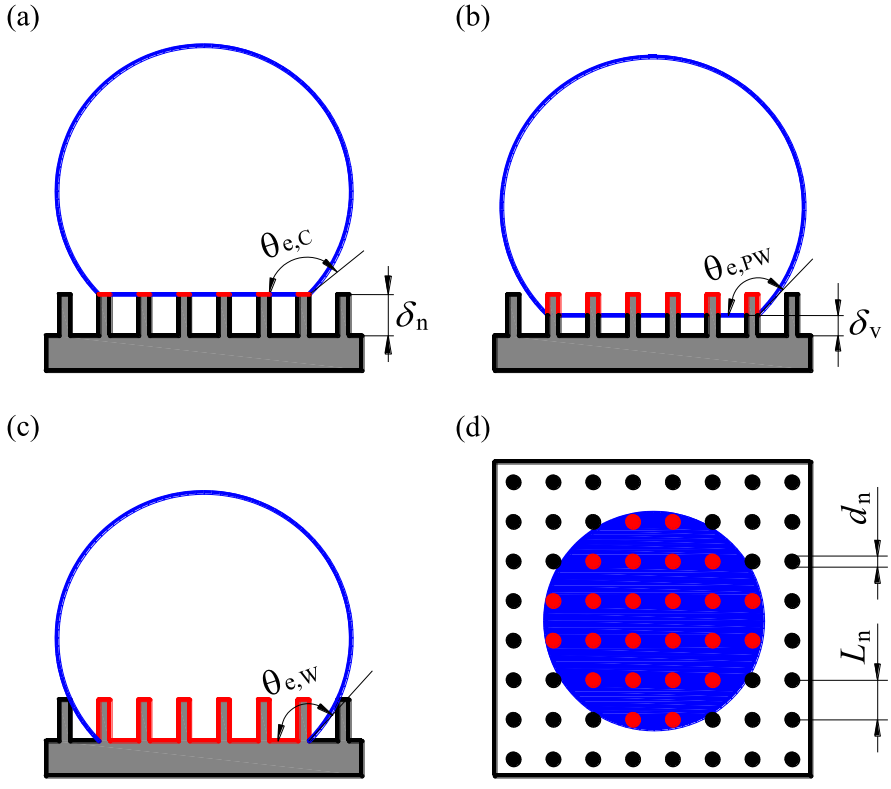

Fig. 2. Three droplet wetting morphologies (a: Cassie state; b: partial Wenzel state; c: Wenzel state; d: top view of nano pillars structure).

$$N(r) = \frac{1}{3\pi r^2 r_{max}} \left(\frac{r_{max}}{r}\right)^{\frac{2}{3}} \tag{19}$$

Small drops grow by condensation from r_{min} to r_c at which coalescence takes place, drops go through different sizes. If an arbitrary size range, say r_1 to r_2, is considered, then, the number of drops entering that size range equals to the number of droplets leaving by growth and the number of drops swept by larger drops. The population balance theory finally yields $n(r)$ as

$$n(r) = \frac{r}{3\pi r_c^3 r_{max}} \times \frac{r_c - r_{min}}{r - r_{min}} \times \frac{A_2 r + A_3}{A_2 r_c + A_3} \times \left(\frac{r_{max}}{r_c}\right)^{\frac{2}{3}} \times \exp(B_1 + B_2) \tag{20}$$

where A_2 and A_3 can be seen in Eqs. (16), (17), B_1 and B_2 are as follows:

$$B_1 = \frac{A_2}{A_1 \tau}\left[r_{min}(r_c - r) + \frac{r_c^2 - r^2}{2} + r_{min}^2 \ln\left(\frac{r_c - r_{min}}{r - r_{min}}\right)\right] \tag{21}$$

$$B_2 = \frac{A_3}{A_1 \tau}\left[r_c - r + r_{min} \ln\left(\frac{r_c - r_{min}}{r - r_{min}}\right)\right] \tag{22}$$

In Eqs. (21) and (22), the sweeping period τ is calculated as

$$\tau = \frac{3r_c^2 (A_2 r_c + A_3)^2}{A_1 (11A_2 r_c^2 - 14A_2 r_c r_{min} + 8A_3 r_c - 11A_3 r_{min})} \tag{23}$$

Up to now, we have completed all the necessary expressions to compute heat flux q and heat transfer coefficient $h = q/\Delta T$. Revisiting part I of this paper series, condensation experiment on SSML has following parameters: $T_s = 333.15$ K, $\sigma = 0.066228$ N/m, $\rho_l = 983.13$ kg/m^3, $\rho_v = 0.13075$ kg/m^3, $h_{lv} = 2357.5$ kJ/kg, $\sigma_c = 1$, $M = 0.018$ kg/mol, $R = 8.3144$ J/mol/K, $\lambda_l = 0.6544$ W/m/K, $\lambda_p = 0.2$ W/m/K, $\delta_p = 1$ nm, $\theta_e = 110.0°$, $\theta_r = 105.4°$ and $\theta_a = 120.6°$.

We note that N_c influences dropwise condensation heat transfer. The sensitivity of the effect of N_c on condensation heat flux q and heat transfer coefficient h is shown in Fig. 1d and e. It is shown that the predicted q and h using $N_c = 2.5 \times 10^{11}$ m^{-2} match our experimental data well. Thus, $N_c = 2.5 \times 10^{11}$ m^{-2} is used as a reference value for condensation heat transfer on SSML, which is also recommended by Kim and Kim [11].

We note that Fig. 1 compares our experimental data on flat surface with model predictions. The comparison is actually performed using the well-established model, which is also used by Refs. [4,9,19]. Our new contribution is to develop a dropwise condensation model on nano-structured surface, incorporating the treatment of drop morphologies and three drop detachment modes etc.

2.3. Dropwise condensation on nanostructure surface

Dropwise condensation on nanostructure surface challenges the treatment of drop wetting morphology, droplet detachment mode and thermal resistance in nano-porous layer. The model of these phenomena is in infancy stage, which should be paid more attention.

2.3.1. Improved droplet wetting morphology model

Contact angle influences drop detachment, drop size distribution and heat transfer. The droplet lifetime from nucleation to detachment is divided into four stages. The first stage involves drop nucleation and growth on a single-nanograss with $r_{min} \ll L_n$, where L_n is the nano-pillars spacing. Liu and Cheng [25] noted drop nucleation starting from zero contact angle (CA) to indicate initial nucleation as an ultra-thin liquid film. Then, the drop grows with increased CA, until CA reaches $\theta_{a,p}$, where $\theta_{a,p}$ is advancing contact angle on an ideal smooth surface. The second stage refers to drop

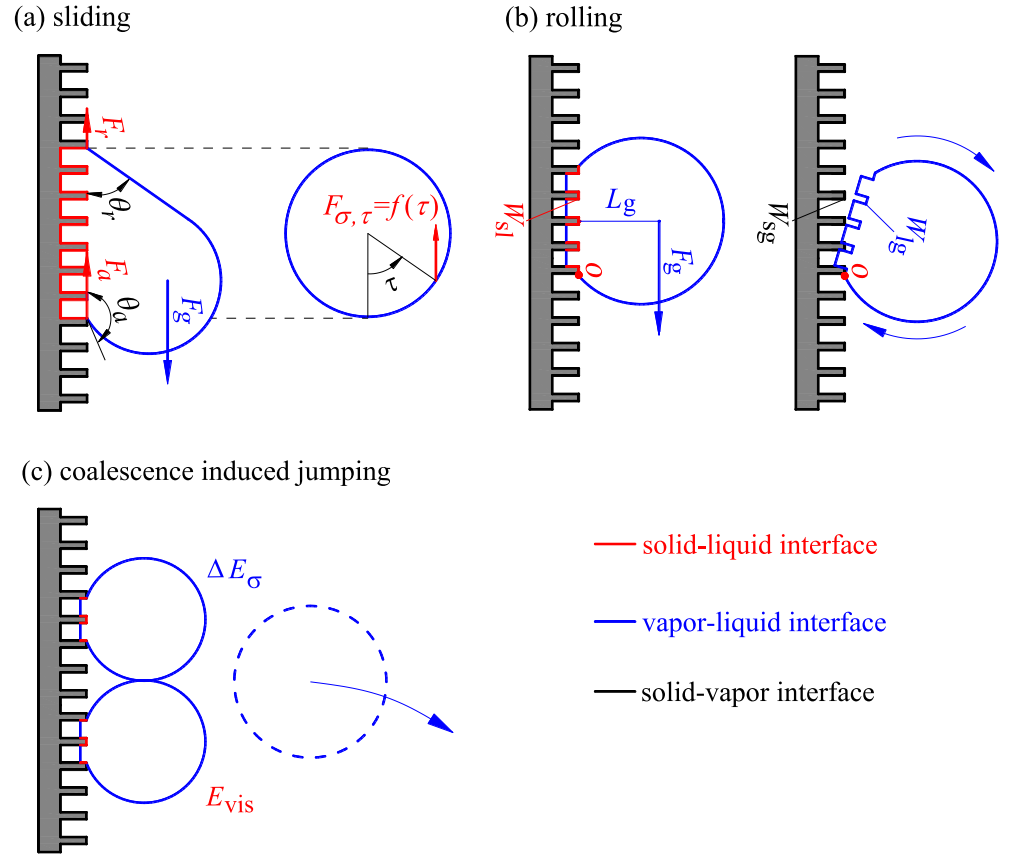

Fig. 3. Three droplet detachment modes.

growth with constant CA = $\theta_{a,p}$, but the contact radius is increased until $r = L_n$, where r is drop radius. The third stage refers to drop growth when crossing from a single-nanograss to neighboring nano-grass, during which CA is sharply increased from $\theta_{a,p}$ to θ_e. The fourth stage is the drop growth on multi-nanograsses with constant CA. Both the first and third stages have varied contact angles, but last very short time compared with the entire drop lifetime [26]. For the second and fourth stages, the constant-contact-angle droplet growth is observed by ESEM (Environmental Scanning Electron Microscopy) [6,27]. The constant-contact-angle droplet growth contributes dominant time compared with the whole droplet lifetime. Thus, previous studies also treated the droplet growth at constant contact angle [11–16].

In this paper, the first and second stages are combined into a constant-contact-angle stage with CA = $\theta_{a,p}$. The third and fourth stages are combined into a constant-contact-angle stage with CA = θ_e. This section describes the judgement of specific drop morphology (Cassie, Wenzel, or partial Wenzel) and the determination of θ_e at corresponding morphology. Fig. 2 shows contact angles $\theta_{e,C}$, $\theta_{e,PW}$, $\theta_{e,W}$, where the subscript C, PW and W mean Cassie, partial Wenzel and Wenzel, respectively. Nanograsses have a height of δ_n, a diameter of d_n and nanowires spacing of L_n. Enright et al. [28] proposed a morphology criterion as

$$E^* = \frac{-1}{f\cos\theta_{a,p}} \tag{24}$$

where f is the surface roughness. Referring to Fig. 2d, f is

$$f = \begin{cases} 1, & r \leqslant L_n \\ 1 + \dfrac{\pi d_n \delta_n}{L_n^2}, & r > L_n \end{cases} \tag{25}$$

The surface roughness f influences droplet morphology (Cassie, Wenzel, or partial Wenzel). The case $r < L_n$ corresponds to a droplet inside the nano-structure, which is treated as the droplet on a flat surface without nano-structure, where r is the droplet radius, L_n is the nano-pillars spacing. The roughness f is equal to 1. The concept of Cassie or Wenzel is not necessary. Contact angle is enough to characterize the droplet motion. However, for a droplet having $r > L_n$, f is larger than 1. The droplet morphology should be considered. A Wenzel morphology is expected when $E^* > 1$, because the contact line overcomes the energy barrier to depin. Otherwise, $E^* < 1$ causes Cassie or partial Wenzel morphology, because complete depinning is not possible.

Based on Miljkovic et al. [15], contact angle on nanostructure surface at Cassie state is

$$\cos\theta_{e,C} = \varphi(\cos\theta_{a,p} + 1) - 1 \tag{26}$$

where φ is the ratio of nanograsses project area to the droplet project area on substrate:

$$\varphi = \begin{cases} 1, & r \leqslant L_n \\ \dfrac{\pi d_n^2}{4L_n^2}, & r > L_n \end{cases} \tag{27}$$

The treatment of φ into two branches ($r < L_n$ and $r > L_n$) characterizes the droplet inside the nano-structure and standing on the nano-structure surface, respectively, which is similar to the treatment of f in Eq. (25). The values of φ also affects the single droplet heat transfer rate. The contact angle at Partial Wenzel state is

$$\cos\theta_{e,PW} = \begin{cases} \theta_{a,p}, & r \leqslant L_n \\ \dfrac{\pi}{2} + \cos^{-1}\left(\dfrac{L_n}{r}\right) & L_n < r < \dfrac{L_n}{\sin(\pi - \theta_{e,C})} \\ \theta_{e,C}, & r \geqslant \dfrac{L_n}{\sin(\pi - \theta_{e,C})} \end{cases} \tag{28}$$

Finally, contact angle at Wenzel state is

$$\cos\theta_{e,W} = f\cos\theta_{e,p} \tag{29}$$

Eq. (24) may overestimate the wetting state at small supersaturations, namely, even though condensed droplets on a nanostructure surface appeared in a composite state, the calculated E^* might be greater than 1 [29]. The physical details of an emerging droplet morphology and evolution process could not be reflected by this equation [29]. Incorrect trend is predicted by Eqs. (26) and (29), namely, contact angles of Wenzel sate by Eq. (29) may be larger than those of Cassie state by Eq. (26), which is against our common knowledge. For example, for our fresh NGS reported in part I of this paper series, $d_n = 200$ nm, $L_n = 0.8$ μm, $\delta_n = 4$ μm, $E^* = 0.406 < 1$ indicates Cassie sate, Eq. (26) gives $\theta_{e,C} = 167.3°$. The long-term operation yields increased L_n such as $L_n = 1.2$ μm, Eq. (26) gives $\theta_{e,C} = 171.5°$ ($E^* = 0.729 < 1$), which is larger than $\theta_{e,C} = 167.3°$ for fresh NGS. Our experimental observation does not support the increased contact angle after long-term operation. Thus, the droplet wetting morphology model should be improved. Here, the measured contact angle at Cassie state ($\theta_{e,C}$) is used. Contact angles at Wenzel state ($\theta_{e,W}$) are only calculated by Eq. (29) if they are smaller than the measured values. At Wenzel state, once $\theta_{e,W}$ is known, we suggest following expressions to calculate advancing contact angle $\theta_{a,W}$ and receding contact angle $\theta_{r,W}$.

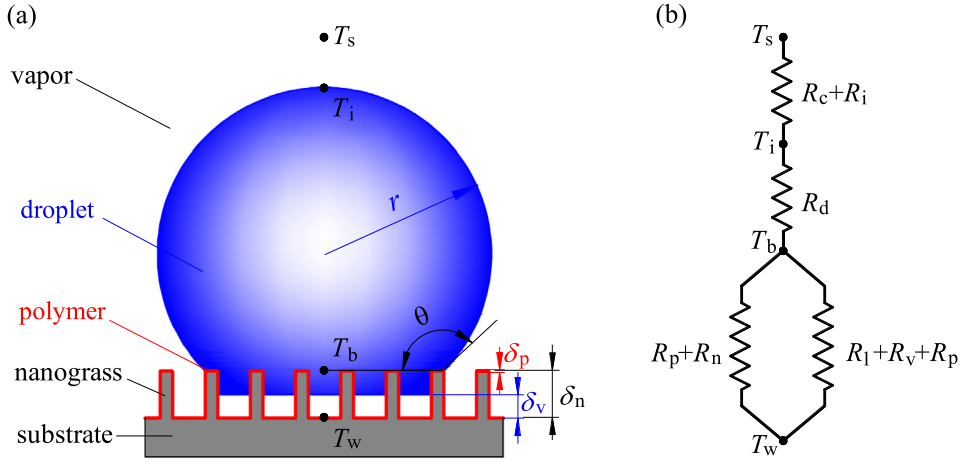

Fig. 4. Thermal resistance network of a single condensate droplet growing on NGS.

$$\frac{\theta_{e,W}-\theta_{e,p}}{\theta_{a,W}-\theta_{a,p}}=\frac{\pi-\theta_{e,p}}{\pi-\theta_{a,p}} \tag{30}$$

$$\frac{\theta_{e,W}-\theta_{e,p}}{\theta_{r,W}-\theta_{r,p}}=\frac{\pi-\theta_{e,p}}{\pi-\theta_{r,p}} \tag{31}$$

where $\theta_{e,p}$, $\theta_{a,p}$ and $\theta_{r,p}$ are equilibrium contact angle, advancing contact angle and receding contact angle, respectively on ideal smooth polymer surface. Eq. (29), together with our newly proposed Eqs. (30) and (31), reflect correct trend, namely, the nanostructure surface raises equilibrium contact angle and reduces the contact angle hysteresis of $\cos\theta_r-\cos\theta_a$.

2.3.2. Mixed droplet detachment model

In contrast to SSML, NGS has fruitful droplet detachment modes. Here, we propose a new mixed droplet detachment model which is embedded in dropwise condensation heat transfer model. There are three reasons to do so. First, the mixed droplet detachment modes of jumping and rolling are indeed observed on fresh NGS. Second, long-term operation of dropwise condensation on

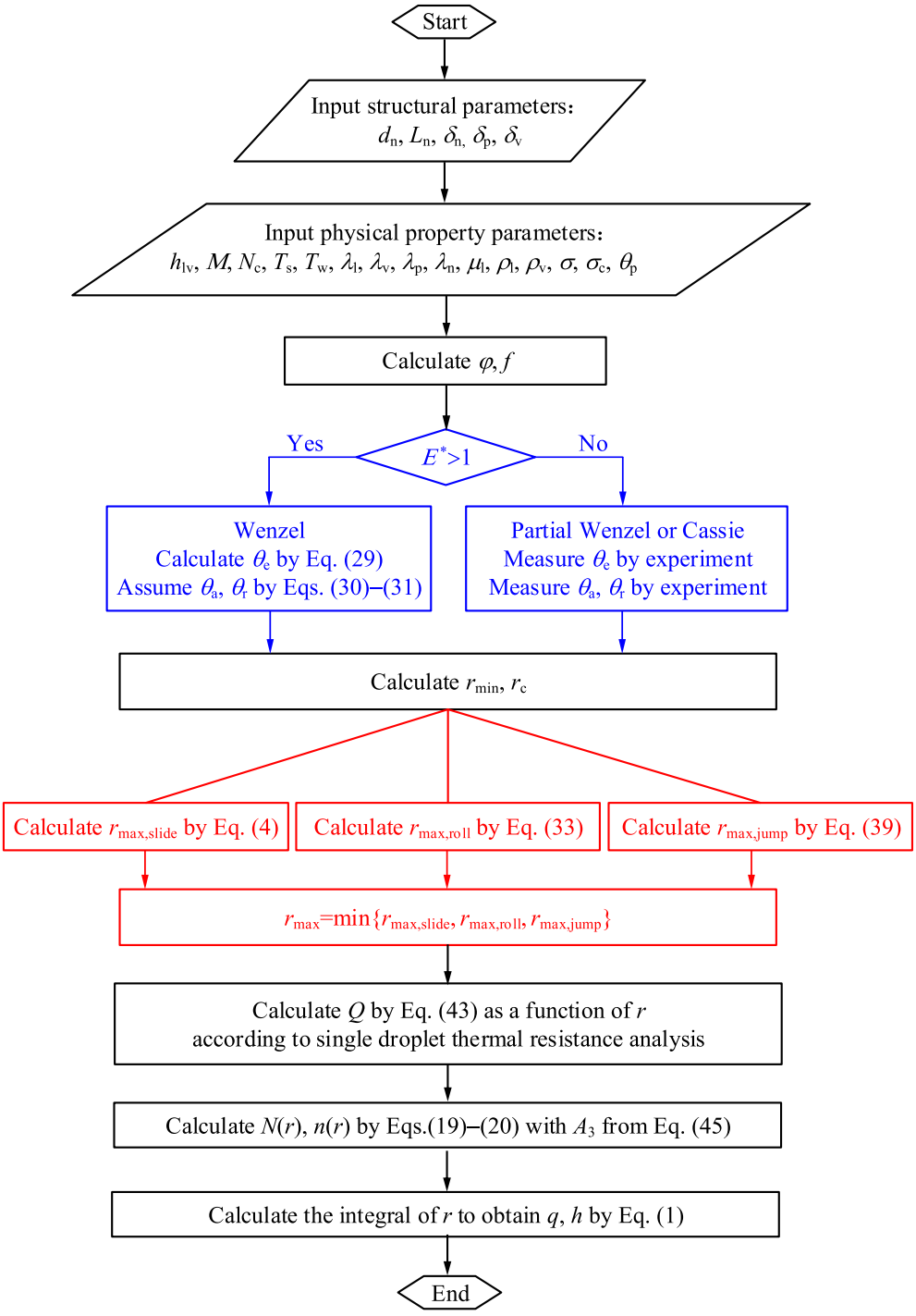

Fig. 5. The computation procedure of dropwise condensation.

NGS changes jumping or rolling mode to sliding mode. Third, under many circumstances, maximum drop radii r_{max} determined by sliding and rolling are in the same magnitude, it is necessary to choose the mode path.

Available condensation heat transfer models only consider sliding mode. Usually, r_{max} related to sliding is developed by force balance between surface tension and gravity [9,10–12]. Rolling, however, is not considered in heat transfer model. Even though many authors highlight the importance of coalescence-induced-jumping to condensation, jumping model is seldom incorporated into condensation heat transfer model.

The three detachment modes are comprehensively considered in this paper (see Fig. 3). The criterion for the determination of r_{max} is

$$r_{max} = \min(r_{max,slide}, r_{max,roll}, r_{max,jump}) \tag{32}$$

where $r_{max,slide}$, $r_{max,roll}$ and $r_{max,jump}$ are maximum drop radii determined by sliding, rolling and jumping, respectively. Our recent work [21] gave theoretical expressions r_{max} for sliding and rolling, from a general sense. For vertical surface and neglecting vapor phase shearing effect on droplets, Eq. (4) determines r_{max} for sliding.

Similarly, for vertical surface and zero shear force from external gas stream, r_{max} for rolling determined by torque balance due to surface tension, gravity and adhesion is [21]:

$$r_{max,roll} = \sqrt{\frac{24}{\pi} \times \frac{(1+\cos\theta_e)(\cos\theta_r - \cos\theta_a)}{3 - 5\cos\theta_e + \cos^2\theta_e + \cos^3\theta_e} \times \frac{\sigma}{(\rho_l - \rho_v)g}} \tag{33}$$

Now we decide coalescence-induced-jumping r_{max}. The simultaneous coalescence of multi-drops yields energy conservation as

$$E_k = \Delta E_s - E_{vis} \tag{34}$$

where E_k is the residual kinetic energy after coalescence, with $E_k < 0$ for no jumping and $E_k > 0$ for jumping, ΔE_s is the surface energy difference before and after coalescence, and E_{vis} is the energy dissipation during coalescence. Based on mass conservation, the merged drop radius r_m is

$$r_m = \sqrt[3]{\frac{1}{4}\sum_{i=1}^{i=J}\left[r_i^3(1-\cos\theta_i)^2(2+\cos\theta_i)\right]} \tag{35}$$

where r_i is the ith droplet radius before coalescence, θ_i is the ith droplet contact angle before coalescence, and J is the number of droplets for coalescence simultaneously. E_{vis} is [30]

$$E_{vis} = 3\kappa\mu_l \sum_{i=1}^{i=J}\sqrt{\frac{\sigma r_i^3}{\rho_l}} \tag{36}$$

where μ_l is the dynamic viscosity of liquid, κ is the dissipation coefficient which is 12. ΔE_s is [31]

$$\Delta E_s = \pi\sigma\sum_{i=1}^{i=J}\left\{r_i^2\left[2 - 2\cos\theta_i + (1 - \phi_{ls} - \phi_{ls}\cos\theta_{e,p})\sin^2\theta_i\right]\right\} - 4\pi\sigma r_m^2 \tag{37}$$

where ϕ_{ls} is the ratio of nano-pillars wetting area to droplet project area on substrate, which is related to wetting morphology:

$$\phi_{ls} = \begin{cases} \dfrac{\pi d_n^2}{4L_n^2}, & \text{Cassie, } \delta_v = \delta_n \\ \dfrac{\pi d_n^2 + 4\pi d_n(\delta_n - \delta_v)}{4L_n^2}, & \text{partial Wenzel, } 0 < \delta_v < \delta_n \\ \dfrac{L_n^2 + \pi d_n \delta_n}{L_n^2}, & \text{Wenzel, } \delta_{v=0} \end{cases} \tag{38}$$

where δ_v is the vapor depth inside the nanograsses under the condensate droplet (see Fig. 2b).

In order to simplify the analysis, r_{max} is determined by the criterion that the residual kinetic energy is zero after the coalescence of two equal sized droplets. Combining Eqs. (34)–(37) yields

$$r_{max,jump} = \frac{36\kappa^2\mu_l^2}{\pi^2\rho_l\sigma(C_1 + C_2)^2} \tag{39}$$

$$C_1 = 4(1-\cos\theta_e) - \sqrt[3]{16(1-\cos\theta_e)^4(2+\cos\theta_e)^2} \tag{40}$$

$$C_2 = 2\sin^2\theta_e(1 - \phi_{ls} - \phi_{ls}\cos\theta_{e,p}) \tag{41}$$

2.3.3. Drop heat transfer rate model

The difficulty in modeling of single drop heat transfer lies in the treatment of thermal resistances in nano-porous layer, which is also related to droplet wetting morphology (see Fig. 4). Resistance at partial Wenzel state is a general treatment. Resistances at Cassie or Wenzel states are the two extreme cases of that at partial Wenzel state. Regarding the nano-porous layer, a single nano-pillar and a spacing between neighboring nano-pillars form a unit. The former has the thermal resistances of $R_n + R_p$, where R_n is the nano-grass resistance such as CuO, R_p is the resistance of the self-assembly polymer layer on nano-grass. The latter has the thermal resistances of $R_l + R_v + R_p$, where R_l is the liquid resistance, R_v is the vapor resistance and R_p is the resistance at the bottom polymer layer. The treatment of thermal resistances network yields

$$R_m = \frac{1}{\frac{1}{R_p + R_n} + \frac{1}{R_l + R_v + R_p}} = \frac{1}{\frac{\varphi\pi r^2\sin^2\theta_e}{\frac{\delta_p}{\lambda_p} + \frac{\delta_n}{\lambda_n}} + \frac{(1-\varphi)\pi r^2\sin^2\theta_e}{\frac{\delta_n - \delta_v}{\lambda_l} + \frac{\delta_v}{\lambda_v} + \frac{\delta_p}{\lambda_p}}} \tag{42}$$

where λ_p, λ_n and λ_v are thermal conductivities of polymer, nano-grass and vapor respectively, δ_p, δ_n and δ_v are polymer layer thickness, nano-grass height and vapor depth respectively, φ is predicted by Eq. (27).

Combining drop curvature resistance R_c in Eq. (5), interface resistance R_i in Eq. (6), drop conduction resistance R_d in Eq. (8) and R_m in Eq. (42) gets

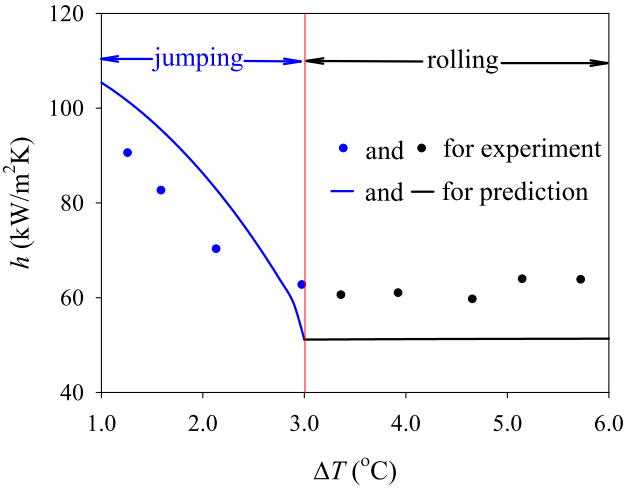

Fig. 6. Comparison of dropwise condensation heat transfer between experiments and predictions on fresh NGS.

$$Q(r)=\frac{\pi r^2(T_s-T_w)\left(1-\frac{r_{min}}{r}\right)}{\frac{1}{2h_i(1-\cos\theta_e)}+\frac{r\theta_e}{4\lambda_l\sin\theta_e}+\left[\frac{\varphi\lambda_n\lambda_p\sin^2\theta_e}{\delta_p\lambda_n+\delta_n\lambda_p}+\frac{(1-\varphi)\lambda_l\lambda_v\lambda_p\sin^2\theta_e}{(\delta_n-\delta_v)\lambda_v\lambda_p+\delta_v\lambda_l\lambda_p+\delta_p\lambda_l\lambda_v}\right]^{-1}} \tag{43}$$

$$G=\frac{\left[\rho_l h_{lv}(1-\cos\theta_e)^2(2+\cos\theta_e)\right]^{-1}(T_s-T_w)\left(1-\frac{r_{min}}{r}\right)}{\frac{1}{2h_i(1-\cos\theta_e)}+\frac{r\theta_e}{4\lambda_l\sin\theta_e}+\left[\frac{\varphi\lambda_n\lambda_p\sin^2\theta_e}{\delta_p\lambda_n+\delta_n\lambda_p}+\frac{(1-\varphi)\lambda_l\lambda_v\lambda_p\sin^2\theta_e}{(\delta_n-\delta_v)\lambda_v\lambda_p+\delta_v\lambda_l\lambda_p+\delta_p\lambda_l\lambda_v}\right]^{-1}} \tag{44}$$

$$A_3=\frac{1}{2h_i(1-\cos\theta_e)}+\left[\frac{\varphi\lambda_n\lambda_p\sin^2\theta_e}{\delta_p\lambda_n+\delta_n\lambda_p}+\frac{(1-\varphi)\lambda_l\lambda_v\lambda_p\sin^2\theta_e}{(\delta_n-\delta_v)\lambda_v\lambda_p+\delta_v\lambda_l\lambda_p+\delta_p\lambda_l\lambda_v}\right]^{-1} \tag{45}$$

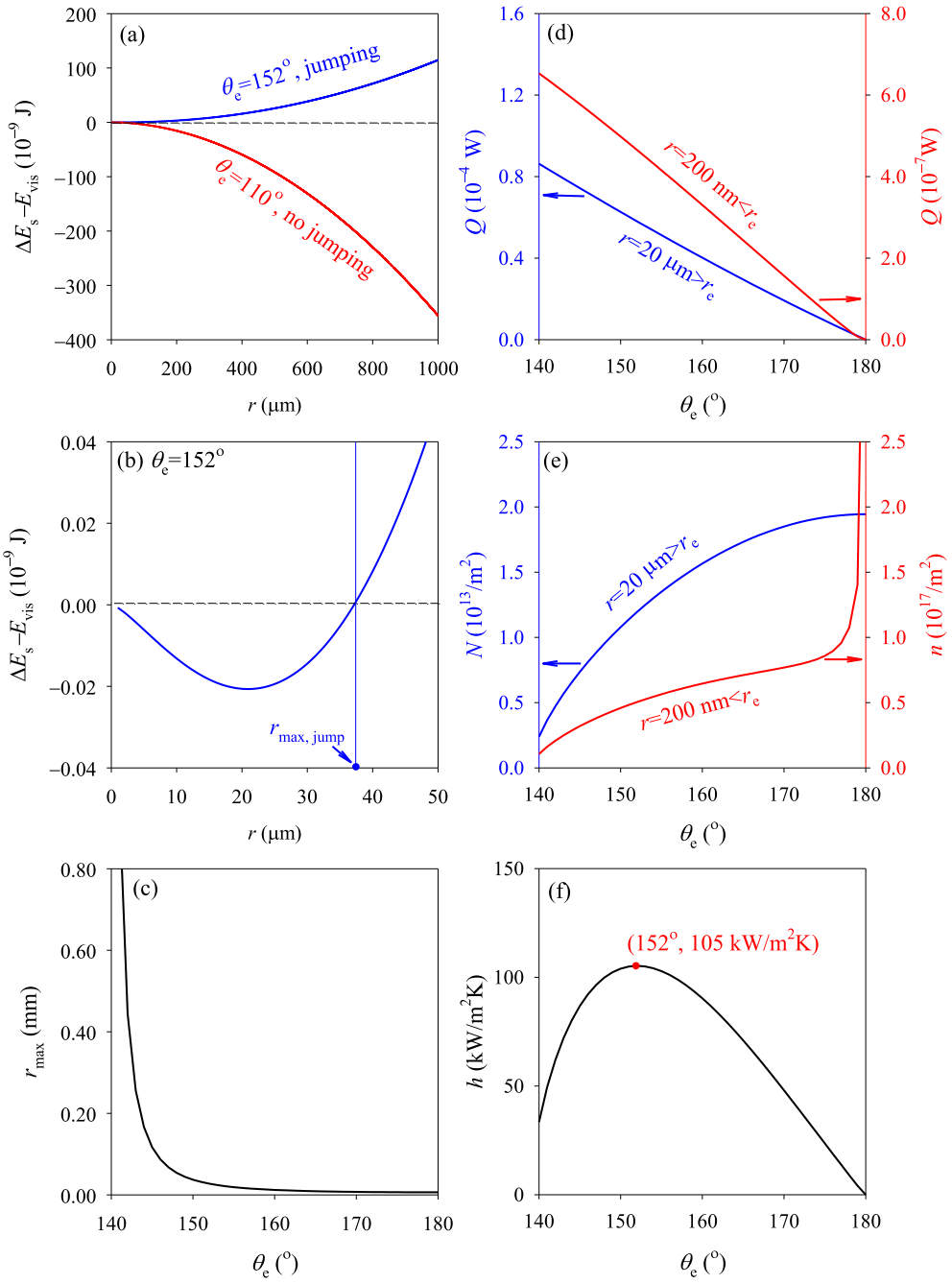

Fig. 7. Effect of contact angle θ_e on droplet detachment radius r_{max} and condensation heat transfer coefficient h in jumping mode ($\phi_{ls}=3$ in all subfigures, $\Delta T=2$ °C in subfigures c–f).

2.3.4. The number of droplet nucleation sites and droplets size distribution

Some investigators noted that rough surface increases number of drop nucleation sites to enhance heat transfer [32], but this effect has seldom been considered in dropwise condensation heat transfer model [12,15]. Sikarwar et al. [10] considered nanostructure as extended surface, and treated drop nucleation site density $N_{c,n}$ on NGS as f times of that on SSML as

$$N_{c,n} = fN_{c,p} \tag{46}$$

where f is computed in Eq. (25). Up to now, the dropwise condensation model on nano-pillars surface is complete. Fig. 5 shows the solution procedure for such heat transfer model.

The remaining issue is the droplet size distribution. Eq. (20) predicts $n(r)$ for smaller droplets. Because A_3 is different on SSML and NGS (see Eqs. (17) and (45)), $n(r)$ is different on the two surfaces. For the size distribution of larger droplets, Le Fevre and Rose [24] proposed Eq. (19) based on the geometry-similarity behavior of droplets at different time. The deduction of Eq. (19) is not limited by the type of surface used. Lee et al. [12] indicated that $N(r)$ is not significantly affected by nano-structured surface. Thus, Eq. (19) is still used to calculate $N(r)$ on NGS, similar to the treatment of Refs. [6,15].

3. Results and discussion

3.1. Comparison with experiment

Our dropwise condensation computation on NGS needs three kinds of parameters: physical property parameters, nanostructure parameters and droplet wetting morphology parameters (see Fig. 5), which are identical to experiments. Physical property parameters are T_s = 333.15 K, σ = 0.066228 N/m, ρ_l = 983.13 kg/m^3, ρ_v = 0.13075 kg/m^3, h_{lv} = 2357.5 kJ/kg, σ_c = 1, λ_l = 0.6544 W/m/K, λ_v = 0.0212 W/m/K, λ_p = 0.2 W/m/K, λ_n = 150.0 W/m/K, μ_l = 0.46597 × 10^{-3} Pa·s. Nanostructure parameters are d_n = 200 nm, L_n = 800 nm, δ_n = 4 μm, δ_p = 1 nm. Droplet wetting morphology parameters include θ_e, θ_a, and θ_r at Cassie, partial Wenzel or Wenzel state. These parameters either come from measurement, or from computation described in Section 2.3.1.

Fig. 6 shows that our dropwise condensation model successfully simulates the data trend over the whole wall subcooling range. Both simulations and experiments show that heat transfer can be clarified into two regimes: low subcooling regime ΔT < 3.0 °C and large subcooling regime ΔT > 3 °C. Heat transfer coefficients are very sensitive to wall subcoolings in first regime, but are almost constant in second regime. Over the whole subcooling range, the average deviation, absolute average deviation and standard deviation between predictions and measurements are −3.03%, 15.30% and 16.86%, respectively. In low subcooling regime, our predictions are slightly larger than our measured values. The slight deviation is due to the sweeping effect, which does not exist practically in jumping mode, but is considered in our model reflected in Eq. (20). In large subcooling regime, our predictions slightly underestimate heat transfer coefficients, due to the neglected shear force at droplet vapor-droplet interface in computations, while the experiment is performed in a low vapor velocity environment $u \approx 3$ m/s.

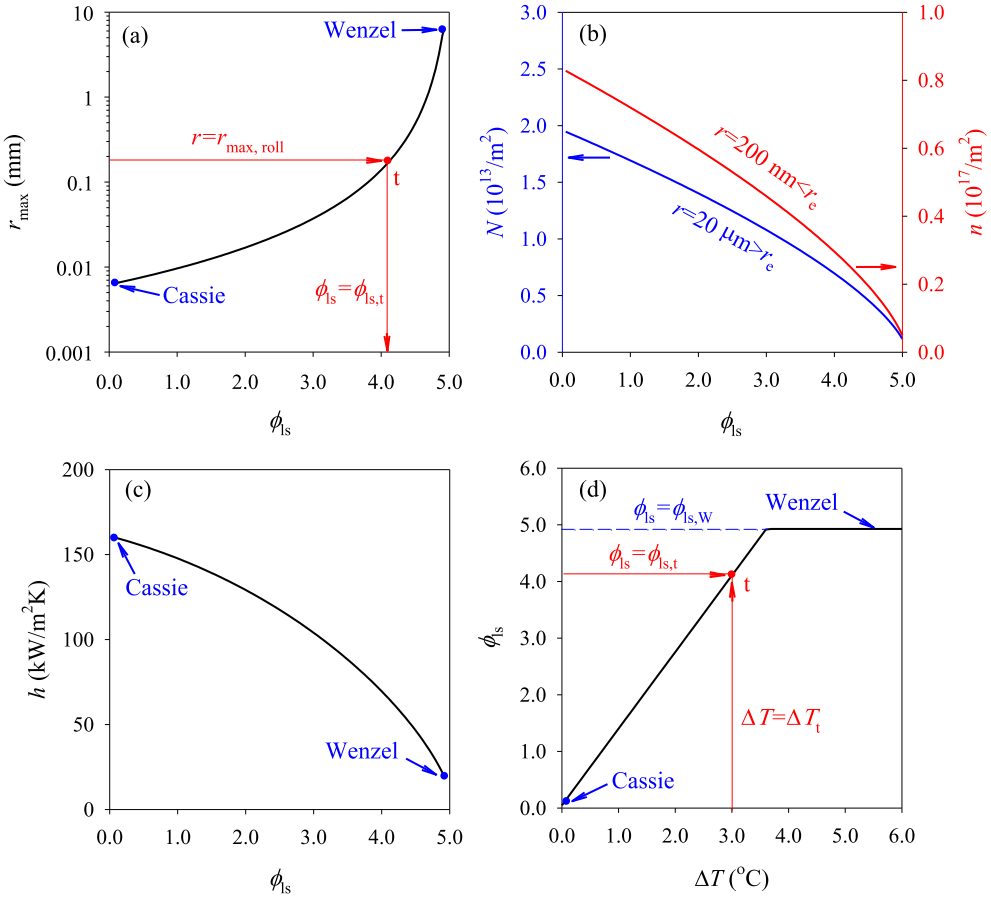

Fig. 8. Effect of nano-pillars wetting area ratio ϕ_{ls} on droplet detachment radius r_{max} and condensation heat transfer coefficients h in jumping mode (θ_e = 152° in all subfigures, ΔT = 2 °C in subfigures b and c).

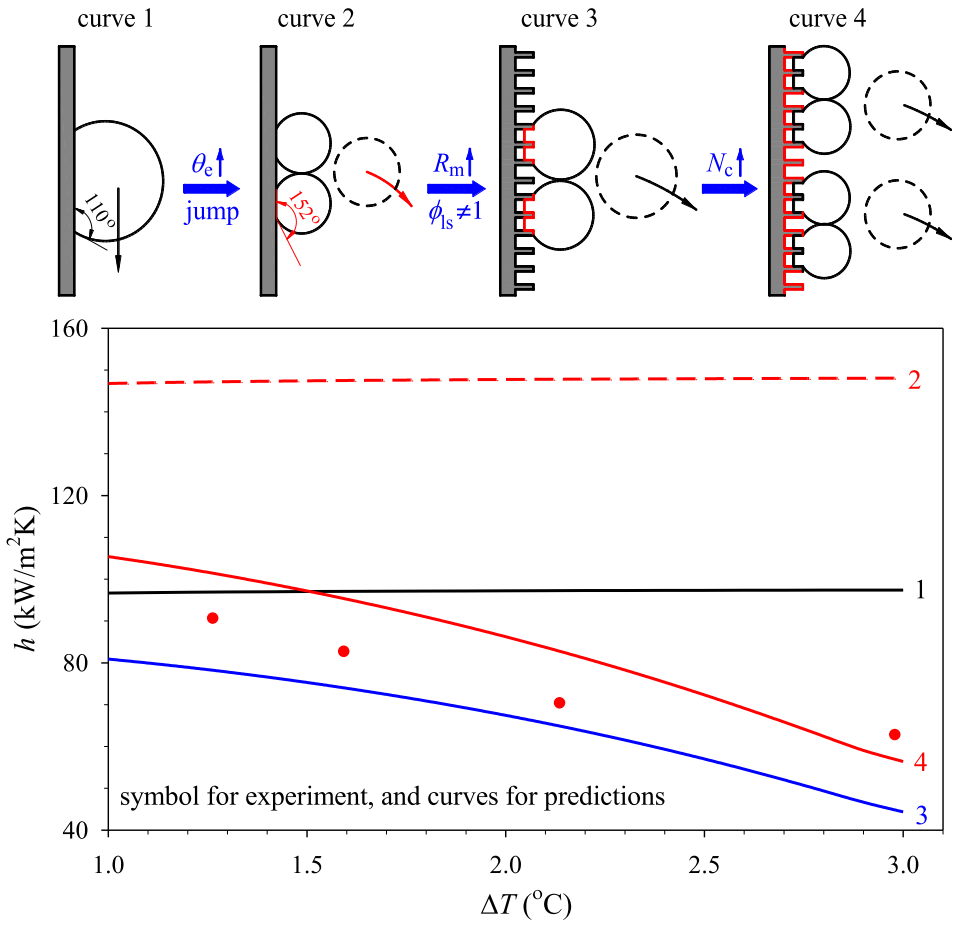

Fig. 9. Summary of nano-structure induced positive and negative contributions to condensation heat transfer in jumping mode.

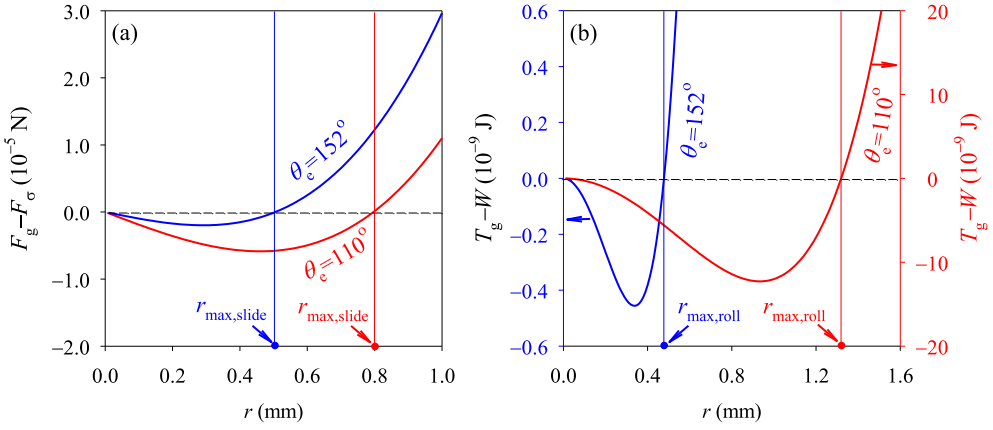

Fig. 10. The definition of r_{max} in sliding and rolling modes ($\Omega = \cos\theta_r - \cos\theta_a = 0.241$).

3.2. Decoupled effect of NGS on dropwise condensation

The value of r_{max}, specifies maximum drop size that can stay on surface, influencing $N(r)$, $n(r)$ and q, see Eqs. (19), (20) and (1). The deductions of $r_{max,jump}$, $r_{max,roll}$ and $r_{max,slide}$ reflect conservations of energy, torque and force, respectively, which are affected by different parameters: θ_e and ϕ_{ls} affect $r_{max,jump}$, θ_e and Ω influence $r_{max,roll}$ and $r_{max,slide}$. Various parameters are decoupled to investigate the separate effect on dropwise condensation in jumping mode (see Figs. 7–9), and rolling or sliding mode (see Figs. 10–13).

3.2.1. Dropwise condensation in jumping mode

Low subcooling regime ($\Delta T < 3.0$ °C) on NGS behaves coalescence-induced-jumping mode, in which r_{max} depends on surface energy difference between before and after coalescence $\Delta E_s \sim r^2$, and energy dissipation during coalescence $E_{vis} \sim r^{1.5}$. Fig. 7a examines residual kinetic energy $E_k = \Delta E_s - E_{vis}$ over a wide r range of 0–1 mm. The jumping criterion is $E_k > 0$. Contact angle strongly influences if a drop can jump. For example, $\theta_e = 152°$ prefers jumping but $\theta_e = 110°$ prefers not jumping. E_k is further plotted focusing on a small r range of 0–50 μm to show parabolic curve

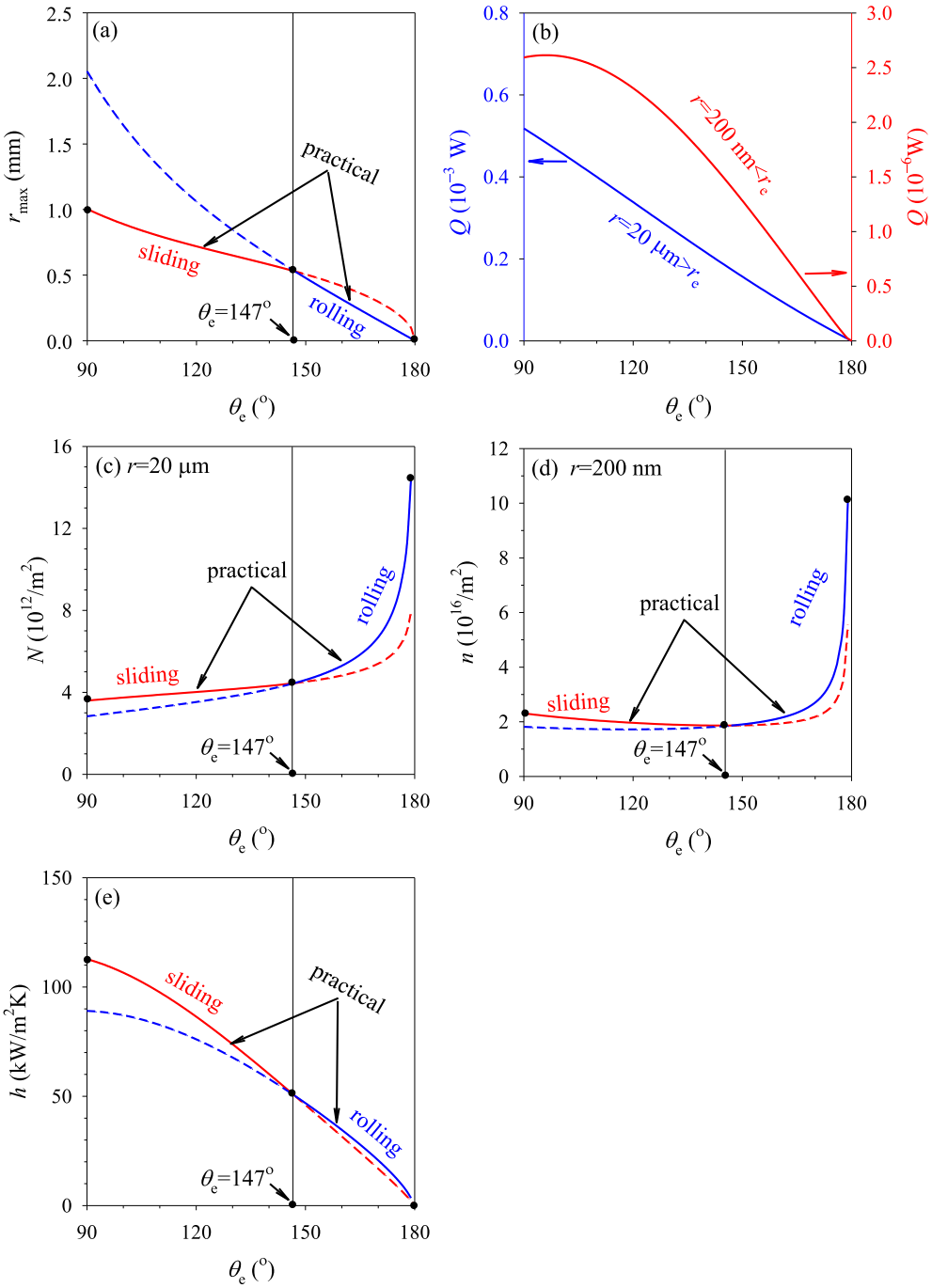

Fig. 11. Effect of contact angle θ_e on droplet detachment radius r_{max} and condensation heat transfer coefficients h in sliding and rolling modes (ΔT = 5 °C, Ω = cosθ_r–cosθ_a = 0.241).

and $r_{max,jump}$ = 38 μm at θ_e = 152° and ϕ_{ls} = 3 (see Fig. 7b). Fig. 7c demonstrates sharp decreased $r_{max,jump}$ with increase of contact angles, especially with θ_e from 140° to 150°.

Compared with SSML, NGS increases θ_e to cause coalescence-induced-jumping and decreased r_{max}. The decreased r_{max} reduces the upper limit of integral for q computation (see Eq. (1)). Besides, heat transfer rate for a single droplet, Q, is decreased by rising θ_e for both large drop and small drop (see Fig. 7d). These two aspects are negative for heat transfer based on Eq. (1).

Now we examine positive effect of increased θ_e on dropwise condensation in jumping mode. By raising θ_e, r_{max} is decreased to increase N due to $N \sim r_{max}^{-1/3}$(see Eq. (19)). There are two routes regarding the effect of θ_e on n. The first route is similar to the relationship between θ_e on N, that is, the rise of θ_e increases n. The second route refers to the effect of θ_e on A_2, A_3, B_1 and B_2 in Eq. (20) to affect n. As a result, Fig. 7e shows the increased N and n with increase of θ_e in jumping mode, which is the positive contribution to heat transfer.

The competition of positive and negative effects yields not monotonic relationship between condensation heat transfer coefficients h and contact angles θ_e. The $h \sim \theta_e$ curve shows a parabola shape, with h_{max} = 105 kW/m^{2}K occurring at θ_e = 152° (see Fig. 7f), at which positive contribution of increased contact angles dominates negative contribution in jumping mode using NGS.

Effect of ϕ_{ls} on dropwise condensation in jumping mode is shown in Fig. 8. Droplet wetting morphology can be characterized by ϕ_{ls}. Cassie state and Wenzel state exist at minimum ϕ_{ls} and maximum ϕ_{ls}, respectively. Fig. 8a shows transition from Cassie state to Wenzel state, and sharply increased $r_{max,jump}$, with continuous increase of ϕ_{ls}. The transition point t is determined by crossing r_{max} curve with the $r = r_{max,roll}$ line, below which drop jumps ($\phi_{ls} < \phi_{ls,t}$), and beyond which drop rolls ($\phi_{ls} > \phi_{ls,t}$). For fresh NGS used in part I of this paper series, $\phi_{ls,t} = 4.105$.

The r_{max} rise induced by the increases of ϕ_{ls} expands the upper limit of integral for q computation shown in Eq. (1), which is the positive contribution to heat transfer (see Fig. 8a). Alternatively, both drop population densities N and n are decreased by increasing ϕ_{ls}, or say r_{max}, which is the negative contribution to heat transfer (see Fig. 8b). The combined effect reflected in Fig. 8a and b yields the decreased condensation heat transfer coefficients versus ϕ_{ls} (see Fig. 8c).

One needs to establish the relationship between ϕ_{ls} and ΔT, assuming the linear relationship between them. For fresh NGS, Cassie state holds the coordinate of (ΔT = 0, $\phi_{ls,C} = 0.049$), and the transition point t from jumping to rolling holds the coordinate of (ΔT = 3 °C, $\phi_{ls,t} = 4.105$), in which the 3 °C subcooling comes from our experiment, and $\phi_{ls,t}$ comes from Fig. 8a. The linear curve is determined by connecting the Cassie state point and the transition point t:

$$\frac{\phi_{ls} - \phi_{ls,C}}{\Delta T - 0} = \frac{\phi_{ls,t} - \phi_{ls,C}}{\Delta T_t - 0} \tag{47}$$

The line is further extended beyond the transition point t, until it intersects with $\phi_{ls,W} = 4.927$ at Wenzel state (see Fig. 8d). The above process determines ϕ_{ls} as

$$\phi_{ls} = \begin{cases} 1.352\Delta T + 0.049 & \text{for } \phi_{ls} < \phi_{ls,W} \\ 4.927 & \text{for } \phi_{ls} = \phi_{ls,W} \end{cases} \tag{48}$$

Coupling Eqs. (38) and (48), the relationship between vapor depth δ_v in nanograsses and ΔT can also be obtained.

We note that, NGS and SSML not only have different θ_e and ϕ_{ls}, but also have different R_m and N_c. Effects of θ_e, ϕ_{ls}, R_m and N_c on the contribution to condensation heat transfer are examined step by step (see Fig. 9), which are described as follows:

Curve 1: Base curve for SSML with $\theta_e = 110°$, $\phi_{ls} = 1$, $R_m = R_p$ and $N_c = 2.5 \times 10^{11}$ m^{-2}.

Curve 2: The curve increases contact angle θ_e to 152° from 110° with other parameters identical to curve 1, showing that the positive contribution is dominant due to increased θ_e and drop jumping on heat transfer. Fig. 7f identifies maximum heat transfer coefficient at $\theta_e = 152°$.

Curve 3: The curve shows strongly negative contribution of nano-porous thermal resistance R_m to heat transfer, where ϕ_{ls} is predicted by Eq. (48), substituting ϕ_{ls} into Eq. (38) yields δ_v to compute R_m by Eq. (42).

Curve 4: The curve shows positive contribution of increased number of drop nucleation sites (N_c) to heat transfer with other parameters identical to curve 3. Curve 4 reflects all positive and

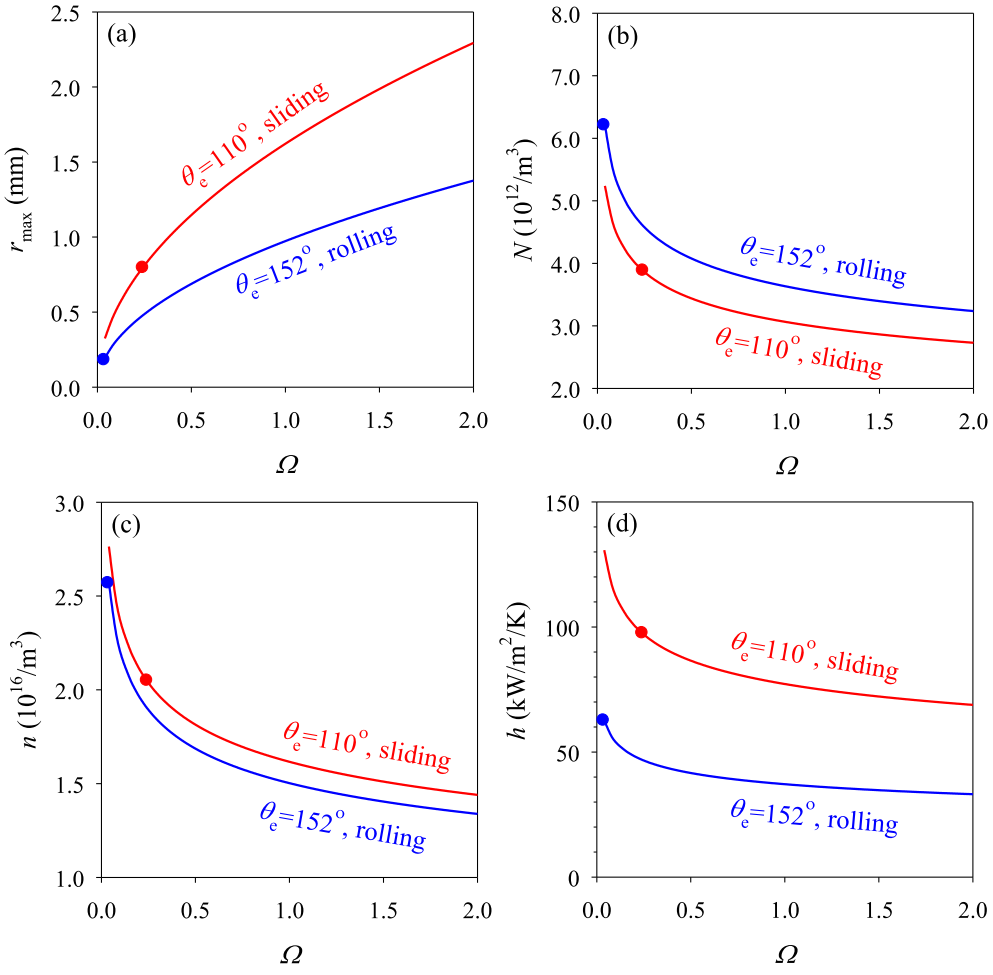

Fig. 12. Effect of contact angle hysteresis Ω on droplet detachment radius r_{max} and condensation heat transfer coefficients h in sliding and rolling modes (ΔT = 5 °C).

negative contributions to heat transfer using NGS in jumping mode.

3.2.2. Dropwise condensation in sliding or rolling mode

At large wall subcoolings $\Delta T > 3.0$ °C, droplets detach fresh NGS in sliding or rolling mode. For vertical surface, onset of sliding is competed by droplet gravity F_g and surface tension F_σ [21]:

$$F_g = \frac{\pi}{3} r^3 (2 - 3\cos\theta_e + \cos^3\theta_e)(\rho_l - \rho_v) g \tag{49}$$

$$F_\sigma = \frac{4}{\pi} r\sigma \sin\theta_e (\cos\theta_r - \cos\theta_a) \tag{50}$$

The criterion $F_g - F_\sigma = 0$ gives r_{max} in Eq. (4). Onset of rolling satisfies the criterion that gravity torque T_g should be larger than adhesion work W due to droplet departure [21]:

$$T_g = \frac{\pi}{12}(3 - 8\cos\theta_e + 6\cos^2\theta_e - \cos^4\theta_e)(\rho_l - \rho_v) g r^4 \tag{51}$$

$$W = 2\sin^2\theta_e (\cos\theta_r - \cos\theta_a)\sigma r^2 \tag{52}$$

The criterion $T_g - W = 0$ gives r_{max} in Eq. (33).

The fact that $F_g \sim r^3$ and $F_\sigma \sim r$ helps to understand r_{max} curves shown in Fig. 10a for sliding. At small r, $F_g - F_\sigma$ is negative, but with increase of r, $F_g - F_\sigma$ is increased to be zero, at which r_{max} occurs thus a drop begins to slide. Similarly, $T_g \sim r^4$ and $W \sim r^2$ yield r_{max} curves shown in Fig. 10b for rolling. One may ask a question: which mode does a droplet prefer, sliding or rolling? In order to answer this question, we plot two r_{max} curves, one for sliding according to Eq. (4) and the other for rolling according to Eq. (33). The two curves are intercrossed at $\theta_e = 147.0°$, which is called the transition contact angle, below which a droplet prefers sliding, and beyond which a droplet prefers rolling (see Fig. 11a). The mode selection parameter I is defined as

$$I = \frac{r_{max,slide}}{r_{max,roll}} = \sqrt{\frac{\sin\theta_e(3 + \cos\theta_e)}{2\pi(2 + \cos\theta_e)(1 + \cos\theta_e)}} \tag{53}$$

I is related to contact angle only. For $I < 1$, $r_{max,slide} < r_{max,roll}$ corresponds to sliding with $\theta_e < 147.0°$. For $I > 1$, $r_{max,roll} < r_{max,slide}$ corresponds to rolling with $\theta_e > 147.0°$.

Fig. 11a shows decreased r_{max} with increase of θ_e. In this study, $\theta_e = 152°$ for fresh NGS switches sliding mode with $\theta_e = 110°$ for SSML to rolling mode, which further reduces r_{max}. The r_{max} decrease lowers the upper limit of integral for q computation shown in Eq. (1), which contributes to heat transfer negatively. The decrease of Q with increase of θ_e behaves another negative contribution (see Fig. 11b).

Because r_{max} depends on θ_e and mode selection between sliding and rolling, drop population density N is increased versus θ_e, following the route shown by solid curves in Fig. 11c, which is a positive contribution to heat transfer. Eq. (20) shows the drop population density n as a function of r_{max}, A_2, A_3, B_1 and B_2, which are all dependent on θ_e. This behavior yields the insensitive n with respect to θ_e variation, except when θ_e is approaching 180°,

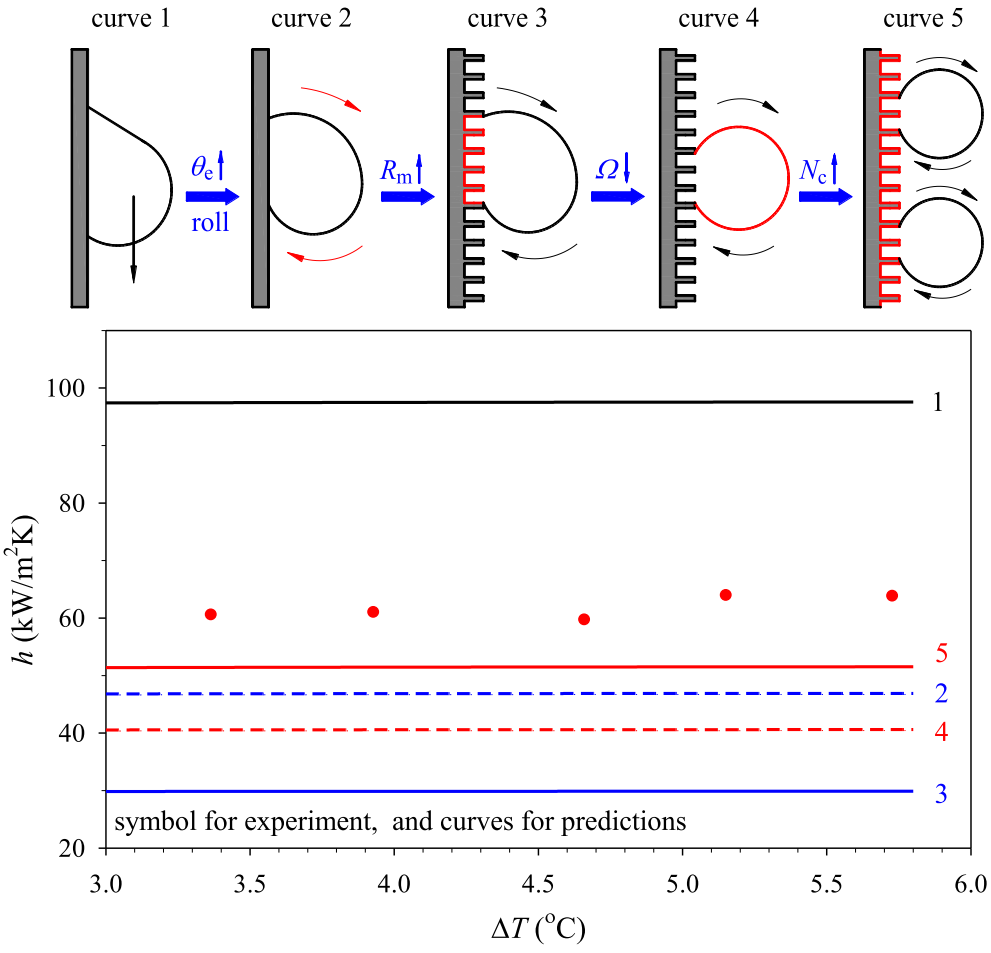

Fig. 13. Summary of nano-structure induced positive and negative contributions to condensation heat transfer in rolling mode.

indicating an almost constant contribution to heat transfer regarding n with respect to θ_e variation (see Fig. 11d).

Based on Fig. 11a–d, the comprehensive effect behaves decreased condensation heat transfer coefficients h with increased θ_e in the range of 90–180° shown in Fig. 11e. The monotonic change of $h \sim \theta_e$ in sliding or rolling mode in Fig. 11e is different from the parabola $h \sim \theta_e$ curve in jumping mode shown in Fig. 7f. This is because when θ_e is changed, the relative contributions of various factors on condensation heat transfer are different in sliding or rolling mode and in jumping mode.

Contact angle hysteresis Ω also influences r_{max} in sliding and rolling mode. Fig. 12a shows the increased r_{max} with increase of Ω. Eqs. (19) and (20) indicate that both population densities of N and n are proportional to $r_{max}^{-1/3}$. Linking this behavior with the relationship between r_{max} and Ω achieves the decreased N and n versus Ω shown in Fig. 12b and c. In the present study, compared with SSML, NGS reduces Ω from 0.241 to 0.035 to generate positive contribution on condensation heat transfer (see Fig. 12d).

Fig. 13 summarizes effect of various factors on condensation heat transfer. SSML had the parameters of $\theta_{e,p} = 110°$, $\Omega_p = 0.241$, $R_{m,p} = R_p$ and $N_{c,p} = 2.5 \times 10^{11}$ m^{-2}. NGS had the parameters of $\theta_{e,n} = 152°$, $\Omega_n = 0.035$, $R_{m,n}$ predicted by Eq. (42), and $N_{c,n} = fN_{c,p}$. They are explored step by step to identify the decoupled effect:

Curve 1: Base curve for SSML.

Curve 2: Heat transfer coefficients are decreased by raising $\theta_{e,n}$ to 152° with other parameters identical to curve 1, showing negative contribution of increased contact angles to heat transfer, see Fig. 11 for explanation.

Curve 3: Heat transfer coefficients are decreased using $R_{m,n}$ instead of R_p with other parameters identical to curve 2, showing negative contribution of added thermal resistance of nano-porous to heat transfer.

Curve 4: The rise of heat transfer coefficients using Ω_n instead of Ω_p with other parameters identical to curve 3 shows positive contribution of decreased contact angle hysteresis to heat transfer, see explanation in Fig. 12.

Curve 5: This curve shows positive contribution of increased number of drop nucleation sites to heat transfer with other parameters identical to curve 4. This curve reflects all positive and negative contributions to heat transfer using NGS.

In this paper, we incorporate the drop sliding and rolling modes in condensation model. The two modes are theoretically identified in Ref. [21]. Fig. 14 shows additional experiment evidence of the two motion modes. SSML and NGS are prepared to perform the experiment, which are identical to those for condensation experiment. Equilibrium contact angles are 110° on SSML and 152° on NGS, respectively. Particle tracking technique judges sliding or rolling motion. By cooling the surface, droplet can be nucleated and growing on the surface. Copper particles (~100 μm size) are sprinkled on drop downstream along the drop motion direction, suppressing the interference of particles on onset of droplet motion. Once a droplet attains a specific size, it slides on SSML (see Fig. 14a) and rolls on NGS (see Fig. 14b). For sliding, there are no particles observed on drop interface. For rolling motion, there are particles on drop interface. The particles are changing angles with respect to the gravity direction.

3.3. Heat transfer analysis after nanostructure failure

In part I of this paper series, we observe the collapse and breakage of nanograsses after long-term operation. The nanostructure failure enlarges nano-pillars spacing L_n. We analyze what happens after the rise of L_n here.

Effect of L_n on θ_e: Surface roughness f is reduced by increased L_n to decrease θ_e (see Eqs. (25) and (29)). Droplet prefers Wenzel state and sliding mode. The decreased θ_e and increased Ω keep larger r_{max} and smaller N and n, which worsen heat transfer. However, the decreased θ_e enhances Q to display a positive contribution to heat transfer.

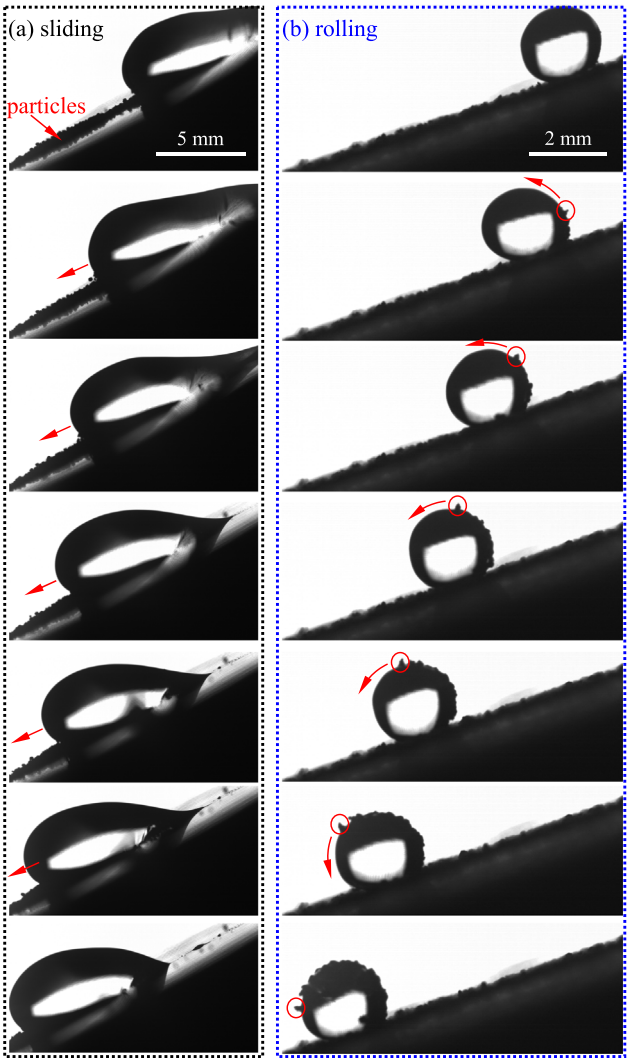

Fig. 14. Direct experiment evidence of sliding and rolling (experiment is performed in 40% humidity wet air environment. a: sliding on SSML with surface inclination angle $\alpha = 30°$, drop volume based radius $r_v = 2.38$ mm and time sequence of 20 ms; b: rolling on NGS with $\alpha = 20°$, $r_v = 1.06$ mm and time sequence of 5 ms).

Effect of L_n on R_m: The solid fraction in nano-porous is scaled as $\varphi \sim L_n^{-2}$. Thus, φ is decreased with increase of L_n to raise thermal resistance of nano-porous R_m (see Eqs. (27) and (42)). This negative contribution is strong due to much smaller thermal conductivities of liquid or vapor than solid.

Effect of L_n on N_c: The number of drop nucleation sites N_c are assumed to have linear relationship with surface roughness f (see Eq. (46)). N_c is reduced to deteriorate heat transfer.

In summary, nanostructure failure increases L_n. Almost all the effects due to the increased L_n are negative, except the enhanced Q. Fig. 15a shows the decreased condensation heat transfer coefficients by raising L_n, during which rolling mode is switched to sliding mode.

Both our experiment and simulation indicate a limit of decayed heat transfer after nanostructure failure (See Fig. 15a). By assuming $L_n \to \infty$ after nanostructure failure, Wenzel state is expected. Condensation heat transfer on NGS after nanostructure failure is almost equivalent to that on a smooth single-molecule-layer of

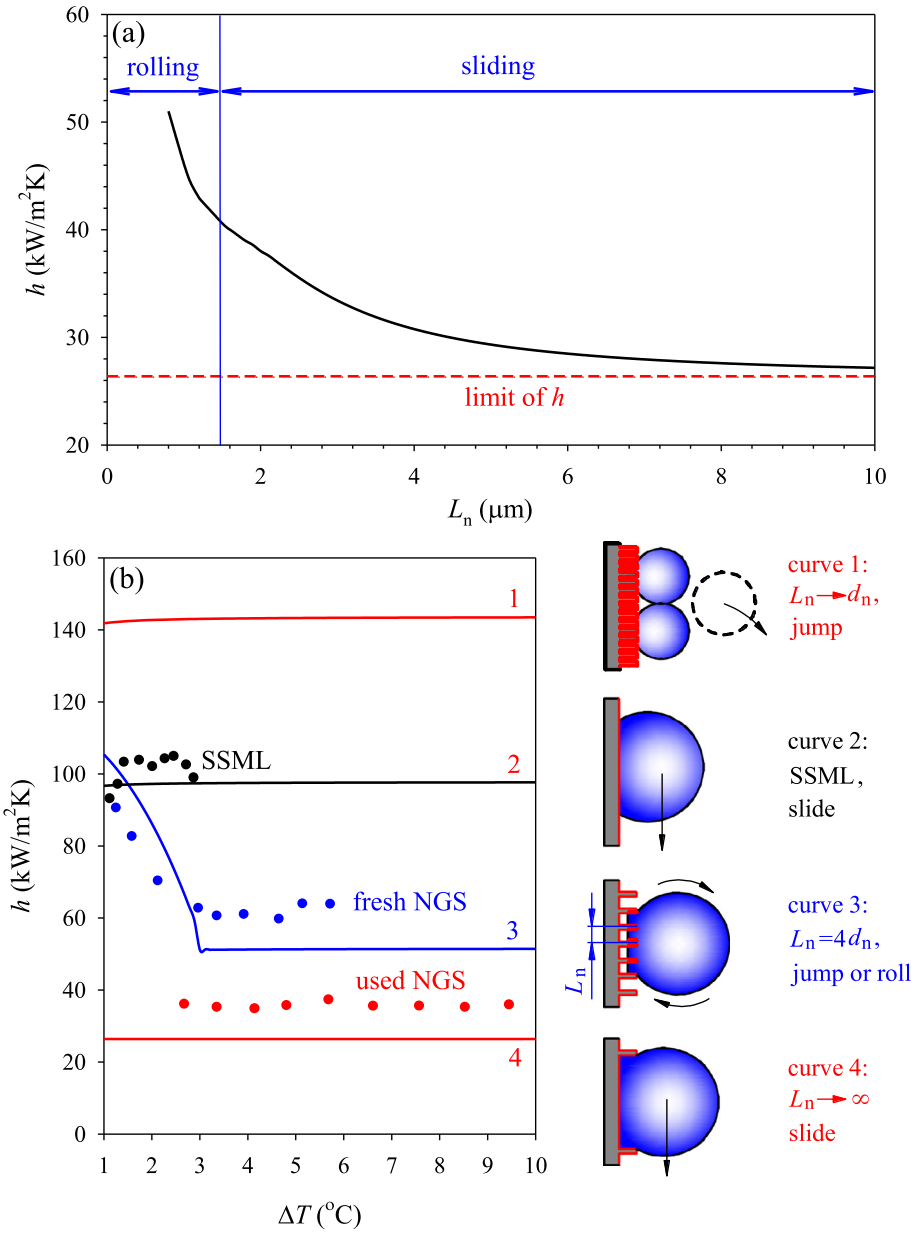

Fig. 15. Effect of nano pillars spacing L_n on dropwise condensation for NGS (a: decreased heat transfer coefficients with increase of L_n due to nanostructure failure, ΔT = 5 °C, d_n = 200 nm, δ_n = 4 μm; b: condensation heat transfer performance on NGS with different L_n, d_n = 200 nm, δ_n = 4 μm).

polymer surface (SSML), due to $f \to 1$, $\varphi \to 0$ and $\theta_{e,w} \to \theta_{e,p}$, see Eqs. (25), (27) and (29). The only difference between NGS after nanostructure failure with $L_n \to \infty$ and SSML is the underneath thermal resistance R_{under}. For SSML, R_{under} is R_p due to polymer layer conduction. However, for NGS after nanostructure failure with $L_n \to \infty$, R_{under} consists of two parts, based on Eq. (42) using φ = 0 and δ_v = 0. The first part is equivalent to R_p. The second part is a thermal conduction resistance induced by the liquid layer with its thickness equivalent to the nanograsses height δ_n. The above treatment is reflected in curve 4 of Fig. 15b.

4. How to design an efficient and robust nanostructure surface?

We developed heat transfer model considering different droplet wetting morphologies and detachment modes. The heat transfer model predicts condensation heat transfer on SSML, fresh NGS and used NGS after long-term operation, matching our experiments reported in part I of this paper series (see curves 2–4 in Fig. 15b). Future work is recommended to optimize dropwise condensation heat transfer on nanostructure surface. Suggestions are proposed as follows.

A larger contact angle and smaller contact angle hysteresis decrease drop detachment sizes to yield high drop population density, which is useful for heat transfer. However, the increase of contact angle worsens single drop heat transfer rate to behave a negative effect. In jumping mode, the positive contribution dominates the negative contribution. In sliding or rolling mode, large contact angle is not good for heat transfer. Thus, jumping mode is preferred to keep better heat transfer performance. We emphasize that, with increase of wall subcoolings, the vapor-liquid interface may penetrate nano-porous to increase nano-pillars wetting area ratio ϕ_{ls} and change jumping into rolling or sliding mode. A better nanostructure surface needs to keep jumping mode over a wider wall subcooling range.

Densely populated nano-pillars are useful to keep jumping mode, reduce additional sublayer thermal resistance and increase the number of droplet nucleation sites, which are key guidance to reach excellent condensation performance. For example, curve 1 in Fig. 15b gives a 40% heat transfer coefficient increment of dense nano-pillars with $L_n \rightarrow d_n$ compared with SSML.

Suggestions are given to resist nanostructure failure. The interaction of solid-liquid-vapor interface opens a new research direction for nanostructure failure. Nano-pillars stress should be analyzed by coupling nanoscale solid mechanics and dynamic vapor-liquid interface. Heterogeneous hydrophobicity/hydrophilicity surface prevents surface from flooding induced by nanostructure failure [33,34]. Because silicon based heterogeneous surface is limited by smaller area [35,36], Xie et al. developed a novel method for large surface fabrication with mesh screen as mask, in which controllable condensation is fulfilled [31]. Droplets are limited within neighboring hydrophilic dots and jump away from surface without shedding, avoiding that *stone rolls on the lawn to spoil the grasses* to resist nanostructure failure. Thus, heterogeneous surface is suggested to keep better condensation performance for long term operation.

5. Conclusions

Following conclusions can be drawn:

- A dropwise condensation model was developed. The relationship between droplet contact angle and wetting morphology is properly treated. A mixed droplet detachment model is proposed to consider jumping, rolling and sliding. Nano-pillars wetting area ratio ϕ_{ls} is correlated with wall subcoolings.
- Our theoretical work predicts heat transfer coefficients on polymer coated surface, fresh nanostructure surface and used nanostructure surface after long-term operation, matching our measured values well.
- Nanostructure surface introduces positive and negative contributions to heat transfer. The increased droplet population density and number of nucleation sites are positive contributions, but the decreased single drop heat transfer rate and additional nano-porous thermal resistance are negative contributions.
- The enlarged nano-pillars spacing after nanograsses failure causes a set of negative effects on heat transfer. Densely populated nano-pillars and jumping mode are recommended to promote condensation performance.
- Nanostructure failure during condensation suggests new interdisciplinary study on nanoscale solid mechanics interacting with vapor-liquid interface. Heterogeneous surface is expected to prevent nanostructure failure for long-term condensation.

Conflict of interest

The authors declared that there is no conflict of interest.

Acknowledgements

The authors thank for the funding support by National Natural Science Foundation of China (51436004) and China Postdoctoral Science Foundation (2017M620712) and Fundamental Research Funds for the Central Universities (2018QN031).

References

[1] N. Miljkovic, R. Enright, Y. Nam, K. Lopez, N. Dou, J. Sack, E.N. Wang, Jumping-droplet-enhanced condensation on scalable superhydrophobic nanostructured surfaces, Nano Lett. 13 (2013) 179–187.
[2] L. Zhong, X.H. Ma, S.F. Wang, M.Z. Wang, X.N. Li, Effects of surface free energy and nanostructures on dropwise condensation, Chem. Eng. J. 156 (3) (2010) 546–552.
[3] H.W. Hu, G.H. Tang, D. Niu, Experimental investigation of condensation heat transfer on hybrid wettability finned tube with large amount of noncondensable gas, Int. J. Heat Mass Transf. 85 (2015) 513–523.
[4] M. Abu-Orabi, Modeling of heat transfer in dropwise condensation, Int. J. Heat Mass Transf. 41 (1) (1998) 81–87.
[5] B.J. Qi, J.J. Wei, L. Zhang, H. Xu, A fractal dropwise condensation heat transfer model including the effects of contact angle and drop size distribution, Int. J. Heat Mass Transf. 83 (2015) 259–272.
[6] N. Miljkovic, R. Enright, E.N. Wang, Effect of droplet morphology on growth dynamics and heat transfer during condensation on superhydrophobic nanostructured surfaces, ACS Nano 6 (2) (2012) 1776–1785.
[7] P. Birbarah, N. Miljkovic, Internal convective jumping-droplet condensation in tubes, Int. J. Heat Mass Transf. 114 (2017) 1025–1036.
[8] X.J. Gong, X.F. Gao, L. Jiang, Recent progress in bionic condensate microdrop self-propelling surfaces, Adv. Mater. 29 (45) (2017) 1703002.
[9] R.F. Wen, Z. Lan, B.L. Peng, W. Xu, X.H. Ma, Droplet dynamics and heat transfer for dropwise condensation at lower and ultra-lower pressure, Appl. Therm. Eng. 88 (2015) 265–273.
[10] B.S. Sikarwar, S. Khandekar, K. Muralidhar, Mathematical modelling of dropwise condensation on textured surfaces, Sādhanā 38 (2013) 1135–1171.
[11] S. Kim, K.J. Kim, Dropwise condensation modeling suitable for superhydrophobic surfaces, J. Heat Transf. 133 (8) (2011) 081502.
[12] S. Lee, H.K. Yoon, K.J. Kim, S.W. Kim, M. Kennedy, B.J. Zhang, A dropwise condensation model using a nano-scale, pin structured surface, Int. J. Heat Mass Transf. 60 (2013) 664–671.
[13] H. Kim, Y. Nam, Condensation behaviors and resulting heat transfer performance of nano-engineered copper surfaces, Int. J. Heat Mass Transf. 93 (2016) 286–292.
[14] R. Enright, N. Miljkovic, N.G. Dou, Y. Nam, E.N. Wang, Condensation on superhydrophobic copper oxide nanostructures, J. Heat Transf. 135 (9) (2012) 091304.
[15] N. Miljkovic, R. Enright, E.N. Wang, Modeling and optimization of superhydrophobic condensation, J. Heat Transf. 135 (11) (2012) 111004.
[16] H.R.T. Bahrami, H. Saffari, Theoretical study of stable dropwise condensation on an inclined micro/nano structured tube, Int. J. Refrig. 75 (2017) 141–154.
[17] C. Graham, G.P. Griffith, Drop size distributions and heat transfer in dropwise condensation, Int. J. Heat Mass Transf. 16 (2) (1973) 337–346.
[18] J.W. Rose, Further aspects of dropwise condensation theory, Int. J. Heat Mass Transf. 19 (12) (1976) 1363–1370.
[19] X.L. Liu, P. Cheng, Dropwise condensation theory revisited Part II. Droplet nucleation density and condensation heat flux, Int. J. Heat Mass Transf. 83 (2015) 842–849.
[20] S. Khandekar, K. Muralidhar, Dropwise Condensation on Inclined Textured Surfaces, Springer, New York, 2014.
[21] J. Xie, J.L. Xu, W. Shang, K. Zhang, Mode selection between sliding and rolling for droplet on inclined surface: effect of surface wettability, Int. J. Heat Mass Transf. 122 (2018) 45–58.
[22] A. Ulman, An Introduction to Ultrathin Organic Films: From Langmuir-Blodgett to Self-assembly, Academic Press, New York, 1991.
[23] G.X. Pang, J.D. Dale, D.Y. Kwok, An integrated study of dropwise condensation heat transfer on self-assembled organic surfaces through Fourier transform infra-red spectroscopy and ellipsometry, Int. J. Heat Mass Transf. 48 (2005) 307–316.
[24] E.J. Le Fevre, J.W. Rose, A theory of heat transfer by dropwise condensation, in: Proceedings of the 3rd International Heat Transfer Conference, vol. 2, 1966, pp. 362–375.
[25] X.L. Liu, P. Cheng, Dropwise condensation theory revisited: Part I. Droplet nucleation radius, Int. J. Heat Mass Transf. 83 (2015) 833–841.
[26] Y.H. Shang, Y.M. Hou, M. Yu, S.H. Yao, Modeling and optimization of condensation heat transfer at biphilic interface, Int. J. Heat Mass Transf. 122 (2018) 117–127.
[27] G.Q. Li, M.H. Alhosani, S.J. Yuan, H.R. Liu, A.A. Ghaferi, T.J. Zhang, Microscopic droplet formation and energy transport analysis of condensation on scalable superhydrophobic nanostructured copper oxide surfaces, Langmuir 30 (48) (2014) 14498–14511.
[28] R. Enright, N. Miljkovic, A. Al-Obeidi, C.V. Thompson, E.N. Wang, Condensation on superhydrophobic surfaces: the role of local energy barriers and structure length scale, Langmuir 28 (2012) 14424–14432.
[29] T.Q. Liu, W. Sun, X.Q. Li, X.Y. Sun, H.R. Ai, Growth modes of condensates on nano-textured surfaces and mechanism of partially wetted droplet formation, Soft Matter 9 (41) (2013) 9807–9815.
[30] X.L. Liu, P. Cheng, X.J. Quan, Lattice Boltzmann simulations for self-propelled jumping of droplets after coalescence on a superhydrophobic surface, Int. J. Heat Mass Transf. 73 (2014) 195–200.
[31] J. Xie, J.L. Xu, Q. Liu, X. Li, Coupling diffusion welding technique and mesh screen creates heterogeneous metal surface for droplets array, Adv. Mater. Interfaces 4 (23) (2017) 1700684.
[32] C.F. Mu, J.J. Pang, Q.Y. Lu, T.Q. Liu, Effects of surface topography of material on nucleation site density of dropwise condensation, Chem. Eng. Sci. 63 (4) (2008) 874–880.
[33] Y.M. Hou, M. Yu, X.M. Chen, Z.K. Wang, S.H. Yao, Recurrent filmwise and dropwise condensation on a beetle mimetic surface, ACS Nano 9 (1) (2015) 71–81.

[34] E. Ölçeroğlu, M. Mccarthy, Self-organization of microscale condensate for delayed flooding of nanostructured superhydrophobic surfaces, ACS Appl. Mater. Interfaces 8 (2016) 5729–5736.
[35] J.J. Bowen, J.M. Taylor, C.P. Jurich, S.A. Morin, Stretchable chemical patterns for the assembly and manipulation of arrays of microdroplets with lensing and micromixing functionality, Adv. Funct. Mater. 25 (2015) 5520–5528.
[36] R. Iino, Y. Matsumoto, K. Nishino, A. Yamaguchi, H. Noji, Design of a large-scale femtoliter droplet array for single-cell analysis of drug-tolerant and drug-resistant bacteria, Front. Microbiol. 4 (2013) 300.